

1

Revision 3

2

Word count: 9808

3

Dissolution-precipitation vs solid-state diffusion in electrum: examples from

4

metamorphosed Au-bearing, volcanogenic massive sulfide (VMS) deposits

5

Haiming Liu^{a,b*}, Georges Beaudoin^{a,b}

6

^a. Département de géologie et de génie géologique, Université Laval, G1V 0A6,

7

Canada.

8

^b. Research Center on the Geology and Engineering of Mineral Resources (E4M),

9

Université Laval, Québec, G1V 0A6, Canada.

10

Abstract

11

Native Au-Ag alloys (electrum) are the predominant precious metal host in

12

Au-bearing volcanogenic massive sulfide (VMS) deposits. The chemical composition

13

and distribution of electrum records crystal growth and post-crystallization processes.

14

In this study, we present detailed textural and compositional data of electrum from the

15

Ming (Canada) and Boliden (Sweden) Au-bearing VMS deposits.

16

Electron probe micro-analyzer (EPMA) and laser ablation-inductively coupled

17

plasma-mass spectrometry (LA-ICP-MS) analyses of electrum enable characterization

18

of chemical zoning in heterogeneous electrum grains. Electrum from Ming exhibits

19

Ag-rich cores, in gradational contact with an outer Au-rich transition zone also

20

enriched in S, Fe, Cu, Zn, and Pb, which is in sharp contact with Ag-rich rims. The

21

textural observations, coupled with *in situ* LA-ICP-MS data, highlight that the

22

electrum zoning arises from a complex interaction between fluid facilitated solid-state

23 diffusion (SSD) within the grain, and coupled dissolution and reprecipitation (CDR)
24 reactions at the grain interface, in response to changing fluid composition and
25 extrinsic parameters, such as temperature, pH, and redox state at Ming. Electrum from
26 Boliden, in contrast, shows a Au-rich core in contact with a gradually increasing
27 Ag-rich rim enriched in Se, Bi, Sb, Te, Sn, S, and Zn, which indicates the formation
28 by fluid facilitated SSD reactions. The different local re-equilibrium caused by SSD
29 from two deposits are attributed to different transport ligands and effects of
30 physicochemical parameters of fluids (e.g., pH and fO_2), resulting in different
31 compositional zoning patterns within electrum. The long-lived metamorphic events
32 that affected the occurrence and compositions of electrum at both VMS deposits,
33 probably provided the elevated temperature and deformation to allow pervasive fluids
34 to remobilize trace metals in electrum, which resulted in the complex chemical zoning
35 in electrum. This study provides insights from *in situ*, textural and chemical analyses
36 to understand the formation of complex chemical zoning in electrum in
37 metamorphosed VMS deposits.

38 **Keywords**

39 Zoned electrum; Dissolution and reprecipitation (CDR); Solid-state diffusion (SSD);
40 Ming; Boliden; Au-bearing VMS.

41 **Introduction**

42 Chemically zoned mineral grains record a time series of reaction conditions
43 experienced by minerals (Spear and Selverstone, 1983). Coupled

44 dissolution-precipitation (CDR) is the most common mineral reaction mechanism in
45 nature (Putnis, 2009; Ruiz-Agudo et al., 2014; Spruzeniece et al., 2017;
46 Konrad-Schmolke et al., 2018; Huang and Beaudoin, 2019; Li et al., 2019a). Coupled
47 dissolution-precipitation reactions result in readjustment of pre-existing mutual
48 grain boundaries under hydrothermal conditions, which has been widely recognized in
49 various geological settings (Tenailleau et al., 2006; Putnis, 2009; Zhao et al., 2009;
50 Zhao et al., 2013; Liu et al., 2017). In hydrothermal systems, complex mineral
51 chemical zoning can be interpreted to reflect chemical changes in fluid compositions,
52 or re-equilibrium related to a number of physicochemical conditions (e.g., Borg et al.,
53 2014). The mechanism of re-equilibration via CDR during fluid-mineral interaction
54 involves the partial or complete dissolution of the parent mineral and reprecipitation
55 of the replacement phase at the interface (Goldsmith and Laves, 1954; Ruiz-Agudo et
56 al., 2014). Recent studies confirm that the chemical composition of placer gold can be
57 modified by repeated episodes of dissolution and precipitation reactions in supergene
58 environments (Reith et al., 2012; Shuster et al., 2017; Melchiorre et al., 2018; Rea et
59 al., 2019; Dos Santos Alves et al., 2020). This mechanism has previously been
60 suggested to explain the formation of electrum with complex zoning textures in
61 hydrothermal systems (Huston et al., 1992; Zhao et al., 2013; Liu et al., 2017; Rosell
62 et al., 2018; Li et al., 2019b).

63 Pseudomorphic replacement reactions, characterized by the preservation of the
64 shape and volume of the replaced minerals, are common in nature during
65 hydrothermal alteration, metamorphism, diagenesis, and chemical weathering (Putnis,

66 2002). However, pseudomorphic replacement in zoned minerals is alternatively
67 attributed to solid-state diffusion reactions (SSD) under hydrothermal conditions,
68 which preserve external morphology and aspects of the crystal structure (Eda et al.,
69 2005; Eda et al., 2006; Putnis, 2009; Xia et al., 2009). Solid-state diffusion reactions
70 controlling the growth of precious metal alloys have been previously reported both in
71 nature (e.g., Au-Ag alloy, Czamanske et al., 1973; Au-Ag-Sb alloy, Zachariáš et al.,
72 2017) and synthetic material studies (e.g., Au-Ag alloy, Hodak et al., 2000; Au-Sn
73 alloy, Baheti et al., 2018; Au-Cu alloy, Xiong et al., 2014). The lack of porosity and a
74 gradational contact between the parent and product phases may be the key
75 crystallographic feature for SSD reactions (Putnis and Putnis, 2007; Zhao et al., 2013).
76 However, a sharp contact instead of a diffusion profile between the parent and product
77 phases is a feature for CDR reactions (Putnis, 2009, 2014; Robert, 2014). Although
78 the microstructures of final products by CDR and SSD are different, the fundamental
79 mechanism remains the same as both involve a re-equilibration of cation exchange
80 (Putnis, 2009).

81 The Au-Ag system forms a complete miscible alloy, according to the
82 Hume-Rothery rules, due to the similar atomic radii, crystal structure, and valence of
83 Au and Ag (Guisbiers et al., 2015). The term *electrum* is used to refer to Au-Ag alloys
84 between 20 wt% and 80 wt% Au, whereas native gold is used for alloys with more
85 than 80 wt% Au (Boyle, 1979). Previous studies have explained Au and Ag solubility
86 during transport and precipitation from fluids based on experimental data (Huston et
87 al., 1992; Gammons and Williams-Jones, 1995; Pal'yanova and Kolonin, 2007).

88 Shikazono and Shimizu, (1987) used Ag/Au ratios of electrum to discuss variations in
89 Eh, pH, temperature, and sulfur contents in auriferous vein deposits. Hagemann et al.
90 (1998) suggested that Ag-rich electrum is related to reduced fluids which reacted with
91 more oxidized ultramafic rocks at the Archean Transvaal gold deposit (Australia).

92 Zoned electrum has been reported in epithermal deposits in the United States, Spain,
93 and Japan (Desborough et al., 1971; Rosúa et al., 2002; Yokoyama et al., 2011).
94 Silver-zoned electrum grains have been investigated in volcanogenic massive sulfide
95 (VMS) deposits in Eastern Australia (Huston et al., 1992) and the Baochun skarn gold
96 deposit (China, Lu et al., 2000). Healy and Petruk (1990) reported zoning of
97 Au-Ag-Hg alloys is a consequence of crystallization of increasingly Ag-rich fluids
98 during retrograde metamorphism at the Trout Lake VMS deposit, Flin Flon (Canada).

99 Gold-bearing VMS deposits are key exploration targets because their gold contents
100 contribute significantly to the ore value (Dubé et al., 2007; Mercier-Langevin et al.,
101 2011). It has been shown that gold can be remobilized from the massive sulfide bodies
102 into veins peripheral to, or within the VMS deposits during deformation and
103 metamorphism (Huston et al., 1992; Tourigny et al., 1993; Sinclair et al., 2000;
104 Larocque et al., 1995). Deformation and metamorphism have been proposed to cause
105 coarsening of gold and upgrading in some VMS deposits (Huston et al., 1992;
106 Årebäck et al., 2005; Wagner et al., 2007; Vikentev, 2016; Mercier-Langevin et al.,
107 2011). However, the effect of metamorphism on electrum compositional zoning still
108 remains unclear.

109 We selected two Au-bearing VMS deposits, Ming (Canada) and Boliden (Sweden),

110 because both have common gold mineralization characteristics: (1) occurrence of
111 zoned electrum, (2) an overlap of VMS and epithermal (Ag, As, Sb, Hg)
112 mineralization with interpreted magmatic contributions (e.g., Bi, Te), (3) complex ore
113 mineralogy with abundant sulfides and sulfosalts, (4) association with
114 andesite-dacite-rhyodacite-rhyolite rocks, and (5) metamorphism and deformation
115 overprints resulting in remobilization of gold (Mercier-Langevin et al., 2011;
116 Mercier-Langevin et al., 2013; Brueckner et al., 2014; Brueckner et al., 2016). Here,
117 we present in situ textural and chemical composition results of electrum from the
118 Boliden and Ming deposits, to investigate compositional zoning characteristics in
119 electrum grains and to constrain the mechanisms responsible for chemical zoning in
120 electrum. Our results provide new insights into how SSD and CDR reactions can form
121 compositional zoning in electrum, and into the effects of metamorphism on precious
122 metal mobility in greenschist to amphibolite facies rocks.

123 **Geology of the selected deposits and sample description**

124 Three electrum-bearing representative samples were selected from the Ming (n=1,
125 Canada) and Boliden (n=2, Sweden) deposits. The geology of the two deposits and
126 their geochemistry are well documented in literature (Bergman Weihed et al., 1996;
127 Wagner et al., 2007; Mercier-Langevin et al., 2013; Pilote and Piercey, 2013;
128 Brueckner et al., 2014; Brueckner et al., 2015; Brueckner et al., 2016; Pilote et al.,
129 2016; Pilote et al., 2020), and only a brief summary is presented here.

130 ***Ming deposit***

131 The Ming deposit is a Cambro-Ordovician bimodal-mafic VMS deposit (3.65Mt at

132 2.26 wt% Cu, 1.13 g/t Au, 6.78 g/t Ag, and 0.32 wt% Zn) located in the northern
133 central part of the Baie Verte Peninsula of Newfoundland (Canada, Pilote and Piercey,
134 2013; Brueckner et al., 2016). The deposit is hosted in the upper part of the Rambler
135 Rhyolite Formation (Figure 1), which is a folded, dome-shaped, sequence of
136 quartz-phyric rhyodacite, quartz-bearing intermediate to felsic tuff and tuff breccia
137 formed during the Cambrian-Ordovician (ca. 487 Ma, Skulski et al., 2010; Pilote et al.,
138 2016). Upper greenschist to lower amphibolite facies metamorphism affected most of
139 Rambler Rhyolite Formation, including four phases of regional deformation (Hibbard,
140 1983; Castonguay et al., 2009). There are five massive sulfide orebodies hosted
141 within variously hydrothermally altered volcanoclastic rocks, which are the 1807,
142 1806, Ming North, Ming South and Lower Footwall zones. The ore mineralogy in the
143 1807 zone consists of (1) pyrite, chalcopyrite, sphalerite, pyrrhotite, arsenopyrite, and
144 galena, (2) uncommon tellurides, selenides, and sulfo-animonides, (3) sulfosalts
145 (tennantite-tetrahedrite), (4) precious metals (electrum, Ag-sulfosalts, and minor
146 silver), and (5) oxides (magnetite, ilmentite, chromite) (Brueckner et al., 2016; Pilote
147 et al., 2016). Precious metal (Au-Ag) emplacement is syngenetic (Brueckner et al.,
148 2014). Gold remobilization and recrystallization during deformation and
149 metamorphism at the Ming deposit is described by Brueckner et al. (2014), Brueckner
150 et al. (2016), and Pilote et al. (2020). Electrum, which occurs along fractures in
151 cataclastic and recrystallized pyrite, and interstitial between recrystallized pyrite ±
152 arsenopyrite, has been interpreted to be the product of Silurian-Devonian
153 metamorphism of pre-existing precious metals at peak temperature up to 500°C

154 (Brueckner et al., 2016).

155 Sample M1807, collected from the massive sulfide orebody in the 1807 zone of the
156 Ming deposit, is composed of pyrite, chalcopyrite, sphalerite, galena, electrum, and
157 native silver. Electrum is the major precious metal alloy, either adjacent to chalcocite
158 or intergrown with bornite and chalcopyrite (Figure 3). Bornite occurs as anhedral
159 grains associated with chalcopyrite and electrum. Native silver predominantly occurs
160 as veins along fractures and between sulfide minerals.

161 ***Boliden deposit***

162 The Boliden deposit is a Au-Cu-As VMS deposit (8.3 Mt at 15.9g/t Au, 50 g/t Ag,
163 1.42 wt% Cu, 0.9 wt% Zn, 0.3 wt%Pb, and 6.8 wt% As) located in the eastern part of
164 the Skellefte district, Sweden (Figure 2), which was formed between ca. 1894 and
165 1891 Ma (Mercier-Langevin et al., 2013). The deposit is hosted in the uppermost part
166 of the rhyolitic metavolcanic Skellefte Group that consists of Early Proterozoic felsic
167 to mafic volcanic rocks with lesser intrusive and sedimentary rocks (Allen et al., 1996;
168 Mercier-Langevin et al., 2013). The Skellefte belt was affected by regional
169 Svecokarelian metamorphism at greenschist to amphibolite grade at ca.1.83-1.81Ga
170 and the peak metamorphic conditions in the Boliden area were estimated as 430°C
171 and 5-7 kbar (Berglund and Ekström, 1980; Billstrom and Weihed, 1996). The ore
172 lenses were flattened and the sulfide assemblages were highly folded and foliated
173 during tectonic deformation (Wagner and Jonsson, 2001; Mercier-Langevin et al.,
174 2013). The main massive sulfide mineralization in Boliden consists of brecciated
175 pyrite, foliated chalcopyrite, fine-grained arsenopyrite, pyrrhotite, and Cu-Pb-Bi-Sb

176 sulfosalts. The pyrite and arsenopyrite are strongly recrystallized and form granular
177 masses or are aligned along foliation (Wagner et al., 2007; Mercier-Langevin et al.,
178 2013).

179 Two typical Au-rich samples were selected from the main massive orebody in
180 Boliden. Sample BLD210 is from the fine-grained massive arsenopyrite ore, whereas
181 sample BLD-1 comes from a chlorite-altered massive pyrite with strong foliation.
182 Electrum is the predominant Au-Ag alloy and is adjacent to arsenopyrite, pyrite, and
183 intergrown with chalcopyrite, whereas native gold was also found as very small
184 (10-20 μm) grains along the boundaries of electrum (Figure 5m).

185 **Analytical methods**

186 Ten polished thin sections from the Ming deposit and twelve from the Boliden
187 deposit, were cut in order to yield significant numbers of electrum grains for study,
188 which were examined by optical microscopy. Backscattered electron (BSE) imaging
189 was used to identify mineralogical and textural relationships using a JEOL JSM-840A
190 scanning electron microscope (SEM) at Université Laval (Canada). The accelerating
191 voltage was 15 kV and the beam current was 60 μA , at a working distance of 20 mm.
192 Electrum grains were analyzed for their major (Au, Ag) and minor elements (Zn, Cu,
193 Co, Fe, Pb, S, Hg, Pt, Se, As) using a CAMECA SX-100 Electron Probe
194 Micro-Analyzer (EPMA) at Université Laval (Canada), equipped with five
195 wavelength-dispersive spectrometers. The analyses used a 25 kV accelerating voltage
196 with 100 nA beam current for minor elements and 20 nA for major elements, both
197 with a 5 μm beam size. Simple oxides (GEO standards block) and pure metals from

198 the Astimex company were used as standard materials. Analysis time was 40 s and 20
199 s of background measurement. Detection limits for each element and precisions
200 calculated from three analyses of gold standard (NA-Au-31) are listed in
201 Supplementary data 1. Electrum compositional maps were obtained by
202 wavelength-dispersive spectroscopy (WDS) X-ray for Au and Ag at an accelerating
203 voltage of 15 kV and a beam current of 100 nA, and a counting time of 20 ms/pixel
204 with a resolution of 577×527 pixels.

205 The trace element analyses of native electrum were carried out at the University of
206 New Brunswick (Canada). Electrum grains were analyzed using a Resonetics
207 S-155-LR 193 nm Excimer laser ablation system coupled with an Agilent 7700x
208 quadrupole ICP-MS. To investigate trace element distributions in electrum, lines were
209 used to ablate across a single grain to generate profiles. A beam size of 10 - 24 μm
210 was used for compositional analysis. Rastering speed for each line was modified
211 based on the beam size to achieve maximum resolution (5 $\mu\text{m/s}$ for 10 μm beam size,
212 8 $\mu\text{m/s}$ for 24 μm beam size). Acquisition time was set to 0.002 s for all the elements
213 resulting in a total sweep time of ~ 0.8 s. Electrum grains were ablated using energy
214 density of 2.3 J/cm^2 , and the beam operating at 10 Hz frequency. Trace element
215 contents, including Mg, Al, Si, Cr, Mn, Fe, Co, Ni, Cu, Zn, As, Se, Pd, Cd, Sn, Sb, Te,
216 Pt, Pb, Bi, Hg, S, Ti, Mo, In, and Tl, were measured by LA-ICP-MS in this study. The
217 external standard NIST610 was used for calibration of Mg, Al, Si, S, Ti, Mo, In, and
218 Tl (Rocholl et al., 1997). The USGS synthetic MASS-1, a pressed powder pellet, was
219 used for calibration of Hg (Wilson et al., 2002). A synthetic gold standard (NA-Au-31)

220 was used for calibration of Cr, Mn, Fe, Co, Ni, Cu, Zn, As, Se, Pd, Cd, Sn, Sb, Te, Pt,
221 Pb, and Bi, whereas a second gold standard (NA-Au-30) was used for quality control
222 of LA-ICP-MS analyses (Milidragovic et al., 2016). The standards were analyzed
223 every eight spots with the same ablation spot size as the unknown sample analysis.
224 Data were reduced using Iolite3.0 software (Longerich, 1996; Paton et al., 2011).
225 Trace element concentrations were internally normalized to Ag values acquired by
226 EPMA at Université Laval. The average detection limit for each element sample and
227 precisions calculated from routine analyses (n=43) of gold standard (NA-Au-31) are
228 reported in Supplementary data 1 and the comparison of routine analyses of trace
229 elements in reference materials (NA-Au-31, NIST610, and MASS-1) by LA-ICP-MS
230 and certificate values is given in Supplementary data 3.

231 **Electrum textures**

232 In massive sulfides from Ming 1807 zone, ten electrum grains from ten thin
233 sections have been investigated and they are either adjacent to, or along fractures in
234 pyrite, and are intergrown with silicates quartz, epidote, or biotite, and sulfides
235 chalcocite, bornite, or chalcopyrite (Figure 3a). Seven of the ten electrum grains are
236 zoned, and they occur as irregular inclusions in bornite, associated with cataclastic
237 pyrite and chalcopyrite (Figure 3b), whereas they can also form anhedral grains and
238 veinlets along the boundaries of chalcocite and bornite (Figure 3c). Native silver
239 occurs as veins or thin films surrounding the electrum grain or along the boundaries of
240 chalcocite (Figure 3c). The internal microstructure of electrum, observed in BSE
241 images, show a light grey core and dark grey rim (Figure 4). Incongruent layers

242 developed towards the electrum margin, between the light grey zone and dark grey
243 rim, and show an abrupt contact (Figures 4 b-f). Several dark grey layers towards the
244 edge of the grain contain more pores than the light grey zone and show various widths
245 in different areas of individual grains (Figures 4 b and c). Within the electrum, the
246 contact between the dark grey core and light grey transition zone, shows a gradational
247 contact (Figures 5a and 6a).

248 At Boliden, twenty-six electrum grains from twelve thin sections were investigated
249 and they occur predominantly as coarse anhedral grains along boundaries of
250 fine-grained, massive, and crystalline arsenopyrite, and at contacts with aurostibite,
251 which are commonly enclosed in quartz in the massive arsenopyrite ore (Figures 3 d
252 and f). Six of twenty-six electrum grains are zoned and occur as veinlets filling in
253 fractures in brecciated pyrite, chalcopyrite, and arsenopyrite in the chlorite-altered
254 massive pyrite ore (Figure 3g). These electrum grains are oriented parallel to the main
255 foliation (Figure 3h). Under BSE, zoned electrum has a light grey core in gradational
256 contact with a dark grey rim (Figures 4 g-i). Fine-grained native gold is not common
257 but can be observed as disseminated grains adjacent to electrum in association with
258 pyrite and chalcopyrite, which is not zoned (Figure 5n). Native silver veins are not
259 observed in the Boliden ore samples. However, fissures transecting electrum both in
260 massive arsenopyrite and foliated pyrite consisted of Ag-rich electrum (Figures 5
261 m-o).

262 **Chemical composition of electrum**

263 The zoned electrum grains were identified in the petrographic and BSE images. To

264 quantify the chemical characteristics of these zoned electrum grains, WDS X-ray
265 maps, EPMA profiles and LA-ICP-MS profiles were used. The major and minor
266 element compositions of electrum grains from Ming and Boliden are presented in
267 Table 1. Chemical composition variations in zoned electrum grains are shown in
268 Figures 5-8.

269 In the 1807 zone of the Ming deposit, zoned electrum grains commonly show a
270 variation in Ag contents from 20 wt% to 40 wt% and Au contents from 62 wt% to 79
271 wt% (Table 1). The WDS X-ray map shows that dark grey cores are Au-poor,
272 surrounded by a light grey transitional zone with higher Au content, and an outer, dark
273 grey, Ag-rich rim (Figure 5b). Profiles across the zoned grain (lines 1 and 3), show
274 that the dark grey core has a high and constant concentration of Ag (24 wt%) and low
275 concentration of Au (75 wt%, Figures 5e). Silver exhibits a progressively decreasing
276 variation from the dark grey core to the rim, whereas Au shows a gradational increase
277 (Figures 6 b and c). There is an abrupt increase of Ag, and decrease of Au, at the light
278 grey transition from grain to the rim (Figure 6b). According to the WDS X-ray map,
279 the Ag-rich rim can be divided into two layers (the inner rim1 and outer rim 2 in
280 Figures 6 a and b). The contact between rims 1 and 2 is sharp in BSE images with an
281 abrupt increase in Ag in rim 2 (Figure 6b). The dark grey core of electrum grains has
282 Au ranging from 65 wt% to 77 wt%, compared to Au in the light grey transition zone
283 ranging from 71 wt% to 78 wt% (Table 1). Gold in dark rims 1 and 2, ranges from 62
284 wt% to 69 wt%, which is lower compared to Au in the dark grey core (65 wt% to 77
285 wt%) and light grey transition zone (71 wt% to 78 wt%). The dark grey core has a

286 range of Ag from 21 wt% to 35 wt%, whereas the light grey transitional zone is
287 relatively depleted in Ag, ranging from 20 wt% to 30 wt%. The average fineness
288 $\{1000 \times \text{Au}_{\text{wt\%}} / (\text{Au}_{\text{wt\%}} + \text{Ag}_{\text{wt\%}})\}$ value in the dark core is 651, which is lower than
289 that in the light grey transitional zone, 761. Rim 1 is dark grey and has an average
290 gold fineness value of 672, compared to rim 2, which has a gold fineness of 609, is
291 slightly darker. Native silver veins filling fractures or along the electrum grain
292 boundaries have up to 99 wt% Ag (Figure 5c).

293 Copper content in the zoned electrum from Ming ranges from 0.03 wt% to 2.9 wt%,
294 shows an increase in concentration from the light grey zone to the dark grey rims
295 (Figures 6 d-f). The dark grey rim 2 has Cu contents of 0.8 wt%, higher than the dark
296 grey core with 0.3 wt%, and light grey transitional zone with 0.1 wt% (Table 1).
297 Sulfur in the dark grey core has an average of 0.05 wt%, a similar amount at 0.06 wt%
298 in the light grey transition, and elevated contents in the dark grey rims up to 0.13 wt%
299 (Table 1). Mercury yields an average 0.7 wt% in the dark grey core, 0.6 wt% in the
300 light grey transition zone, and 0.1 wt% in the dark grey rim (Table 1). Mercury is
301 relatively enriched in the dark grey core and the dark grey rims compared with the
302 light grey zone (Figures 6 d-f). Mercury in Ag-rich veins reaches up to 6.2 wt%,
303 which is lower than the Hg measured in electrum with a range of 8 wt% to 21 wt% in
304 samples from the 1806 zone of the Ming deposit (Brueckner et al., 2014).

305 A LA-ICP-MS profile in a zoned electrum grain from Ming is used to illustrate
306 trace element contents between the dark and light grey zones (Figure 8a and
307 Supplementary data 3). Figure 8b shows that the light grey zone has relatively higher

308 Fe, Cu, Zn, Te, Pb, Bi and S than the dark grey zone, whereas Sn and Sb show similar
309 range and average values.

310 At the Boliden deposit, zoned electrum has a light grey core and a dark grey rim
311 that are coincident with a wide range of Ag concentrations from 6 wt% to 46 wt% and
312 of Au concentrations ranging from 48 wt% to 90 wt% (Table 1). The EPMA spot
313 analyses were arranged along three profiles across the dark and light grey zones in the
314 zoned electrum (Figure 7a). The light grey core has Au concentrations ranging from
315 55 wt% to 90 wt% Au (average 70 wt%) with Au fineness value ranges from 575 to
316 936, whereas the dark rim is Au-poor with a range from 48 wt% to 69 wt% Au
317 (average 61 wt%) with Au fineness values range from 511 to 738 (Figures 5k and 7).
318 In contrast, the Ag concentration in the light grey core ranges from 6 wt% to 40 wt%,
319 whereas Ag is relatively enriched in the dark grey rim, ranging from 25 wt% to 46 wt%
320 (Figure 7). Copper content in the zoned electrum varies from 0.002 wt% to 5 wt%
321 (Figures 7e and f). The light grey core has relatively low Cu, S, and Hg contents with
322 averages of 0.06 wt%, 0.05 wt%, and 1.4 wt%, respectively. The dark grey rim has
323 higher averages of 0.5 wt% Cu, 0.36 wt% S, and 1.9 wt% Hg (Figure 7).

324 A line of LA-ICP-MS spot analyses across the light core to the dark rim is used to
325 investigate trace element variations for the zoned electrum grain from the Boliden
326 deposit (Figure 8c and Supplementary data 3). Generally, the dark grey zone has
327 higher Fe, Cu, Zn, Se, Sn, Sb, Te, Pb, Bi, and S than the light grey zone (Figure 8d).

328 **Discussion**

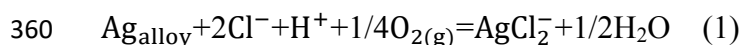
329 The zoned electrum from the Ming deposit is characterized by a Ag-rich core, a

330 gradational contact with a Au-rich transition zone, and an abrupt contact with a
331 Ag-rich rim (Figure 5a). In contrast, the zoned electrum from the Boliden deposit is
332 characterized by a Au-rich core with a gradational contact with a Ag-rich rim (Figure
333 5i), which was previously reported both in massive and vein orebodies in the deposit
334 (Bergman Weihed et al., 1996). The gradational chemical contact was observed in
335 both VMS deposits; however, the abrupt chemical contact is only observed in
336 electrum from the Ming deposit. Zoned electrum in both VMS deposits exhibits an
337 opposite zoning pattern of Au-Ag composition from the core to the margin, which
338 likely records different crystal growth and post-crystallization processes. The content
339 of Au and Ag in electrum grains are controlled by their solubilities in hydrothermal
340 fluids under different conditions (Pal'yanova and Kolonin, 2007). Therefore, different
341 compositional zoning characteristics in electrum likely indicate different precipitation
342 conditions.

343 ***Formation of zoned electrum at Ming***

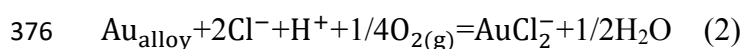
344 At Ming, the close mineralogical association of the Ag-rich electrum core with
345 arsenopyrite, chalcopyrite, pyrrhotite, and sphalerite suggests that Au was transported
346 by bisulfide complexes at a temperature < 300°C, in reduced fluids, whereas the
347 association of Ag-rich electrum rim with galena and chalcopyrite suggests that Ag was
348 transported by chloride complexes (Seward, 1973; Huston et al., 1992;
349 Williams-Jones et al., 2009; Brueckner et al., 2016). The silver-rich electrum core
350 suggests a low pH solution, because silver chloride complexes are far more soluble
351 than the bisulfide complexes at low pH, indicating Ag is more mobile than Au (Mann,

352 1984; Wilson, 1984; Gammons and Barnes, 1989). The formation of electrum grains
353 along fractures in recrystallized pyrite or arsenopyrite has been interpreted to be of
354 syngenetic origin between 260°C to 300°C at Ming, whereas the regional
355 Silurian-Devonian deformation indicates a peak metamorphic temperature of 500°C
356 (Brueckner et al., 2016). At elevated temperature, silver likely tends to be dissolved
357 via reaction (1), leading to the increase in Au content to form the Au-rich zone with a
358 gradational contact with the electrum core (Gammons and Williams-Jones, 1995;
359 Migdisov et al., 1999).

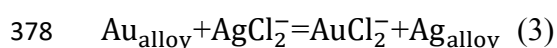


361 The incongruent layers near the Ag-rich margin of electrum at Ming likely
362 indicates dissolution from the core to the margin (Figure 4b). The Ag-rich rim of
363 electrum grains at the Ming deposit precipitated on the exterior of Au-rich zone and
364 exhibits an epitaxial relationship with the parent electrum (Figures 4e and f). The
365 presence of sharp interfaces between the Au-rich zone and Ag-rich rims is generated
366 by repeated coupled dissolution and reprecipitation (Figure 4b and f, Bowell, 1992).
367 The coexisting mineral assemblage of bornite + chalcocite also implies a higher
368 temperature event, because bornite + chalcocite precipitates in oxidized conditions
369 during an input of Cu-rich fluid (> 300°C) in VMS deposits (Hannington, 1999; Koski,
370 2010). The general trend of increasing Ag with Cu composition in the Ag-rich rims
371 likely suggests the later pulse of Cu-rich chloride complex fluid may be rich in Ag
372 and precipitated silver-rich veins in fractures (Figure 9a). Under a decreasing
373 temperature and oxidized condition, the dissolution of Au and reprecipitation of Ag at

374 the interface are facilitated by reaction (2) and (3) to form the sharp compositional
375 contact (Figures 4d and f, Gammons and Williams-Jones, 1995).



377 and



379 In addition, there is an enrichment of S-Fe-Cu-Zn-Pb suite from the Ag-rich core to
380 the Au-rich transition zone at Ming (Figure 11a), likely because these elements were
381 mobilized and readily re-incorporated into electrum from fluids during prograde
382 metamorphism (Lockington et al., 2014). Native silver is not common throughout the
383 Ming deposit because the syngenetic fluids conditions did not favor Ag solubility
384 (Brueckner et al., 2016). Native silver rims precipitated in fractures and along the
385 boundaries of bornite and chalcocite (Figures 3c and 5) are likely remobilized from
386 sulfides under metamorphic conditions due to its high mobility and ductile behavior.
387 Hence, the mobilization of silver from proximal sulfides under low- to medium-grade
388 metamorphic environments favors an upgrading of Ag contents at the rim of electrum.

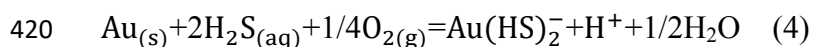
389 It is worth noting that porosity, as an integral microstructural feature of CDR, is
390 essential to sustain fluids to transport and react at the interface between the parent and
391 product phases (Putnis, 2009). The small pores in the incongruent layers in the
392 electrum from Ming, allowing fluids to react with parent electrum, are likely the
393 consequence of CDR at the interface (Figures 4b and c). The generation of grain-scale
394 fractures in parent electrum also provides possible pathways for pervasive transport of
395 fluids to react with the electrum interface, which facilitated CDR, resulting in multiple

396 thin layers of Ag-rich rims (Figure 4b-f). It appears that the compositional zoning in
397 electrum is related to the fractures within the grain, or the grain edge, indicating a
398 post-precipitation re-equilibration (Figures 4 and 5). The existence of nanoscale
399 porosity in electrum will need to be further assessed by transmission electron
400 microscopy.

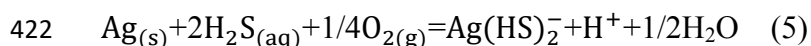
401 *Formation of zoned electrum at Boliden*

402 At Boliden, a gradational contact between the Au-rich core and Ag-rich rim is
403 observed and Ag-rich veins are precipitated in the fractures of electrum (Figures 4h
404 and 5o). The sericite-quartz and sericite-chlorite alteration assemblages and the
405 association of electrum with arsenopyrite ± pyrite ± pyrrhotite indicate a more
406 reduced fluid and gold bisulfide complexes were likely dominant at low temperatures
407 (< 300°C) (Huston et al., 1992; Mercier-Langevin et al., 2013). This reduced fluid
408 contained high H₂S and sufficient HCl to produce the necessary acidity to leach the
409 host rocks to precipitate a large amount of arsenopyrite (Bergman Weihed et al., 1996).
410 At elevated temperature, the solubility of gold in sulfide complexes tends to be
411 sensitive to changes in pH and redox potential (Stefánsson and Seward, 2004). In the
412 presence of electrum, $a_{\text{H}_2\text{S}}$ has significant effects on gold solubility and $f\text{O}_2$ has
413 moderate impacts on gold solubility. The wall rocks of Boliden massive sulfide ore
414 display a zoned alteration pattern with an inner envelope dominated by white mica ±
415 andalusite and outer chlorite ± sericite zone (Bergman Weihed et al., 1996), indicating
416 an acidic fluid responsible for the advanced argillic alteration that precipitated the
417 Au-rich electrum (Marquis et al., 1990). Gold solubility can be increased through

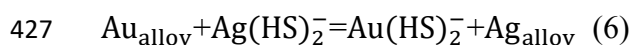
418 reaction (4), and the solubility of Ag can be increased by reaction (5) with decreasing
419 pH in oxidizing fluids (Gammons and Williams-Jones, 1995).



421 and



423 Under elevated temperature ($> 300^\circ\text{C}$, corresponding to the peak metamorphism)
424 and/or $a_{\text{H}_2\text{S}}$, the Au-rich electrum is dissolved via reaction (6) to form a gradational
425 diffusion contact at the interface (Huston et al., 1992; Gammons and Williams-Jones,
426 1995).



428 The general trend of increasing Cu with Ag composition in the Ag-rich rim, likely
429 suggests a later pulse of Cu-rich fluid (Figure 9b). With increasing pH and decreasing
430 temperature, the Ag-rich electrum rim precipitated, coarsening the electrum grain and
431 decreasing gold fineness during retrograde metamorphism. The gradual variations in
432 Au and Ag observed in BSE images, EPMA and LA-ICP-MS line profiles, suggest the
433 SSD of metals is facilitated by reaction (6), across the gradational contact between the
434 light and dark zones (Figures 4, 7, and 8).

435 *Diffusion trends in zoned electrum grains*

436 Opposite diffusion trends are observed in Au-Ag-Cu composition diagrams from
437 each deposit. This suggests that precipitation conditions controlling the zoned
438 electrum compositions in the Ming and Boliden deposits are different (Figure 9). At
439 Ming, the parent electrum core is Ag-rich, and Ag is leached from electrum to form

440 Au-rich electrum, with irregularly gradual contact generated by SSD reactions
441 facilitated by Au-rich, low pH fluids with increasing temperature (Figures 9a and 10b,
442 Hough et al., 2007; Rosell et al., 2018). These fluids seem to be enriched in Fe, Cu,
443 Zn, Te, Pb, Bi and S, and these elements are redistributed and incorporated into
444 electrum during the modification of Ag-rich electrum (Figures 8b, 10b, and 11a). In
445 contrast, the parent electrum is Au-rich at Boliden, and Ag in electrum is soluble and
446 is easy to be mobilized at low pH, under reduced conditions (Figures 10 d and e,
447 Gibert et al., 1998; Williams-Jones et al., 2009). The gradational contact between the
448 Au-rich core and Ag-rich rim, and absence of multiple layers, suggest a SSD reaction
449 that mobilizes Ag from Au-rich electrum, which is slow at 300°C but faster at
450 temperature > 300°C facilitated by Ag-rich fluids (Figure 10f, Huston et al., 1992;
451 Gammons and Williams-Jones, 1995; Marshall et al., 2000). These Ag-rich fluids can
452 also mobilize Fe, Cu, Zn, Se, Sn, Sb, Te, Pb, Bi, and S, and these elements are
453 incorporated in the Ag-rich electrum (Figures 8d, 10e, and 11b).

454 Gammons and Williams-Jones (1995) indicated that electrum precipitation from
455 aqueous sulfide-rich solutions is sensitive to pH, where a drop in pH causes a
456 continuous increase in Au content in electrum, when Au is transported by bisulfide
457 complexes $\{\text{Au}(\text{HS})_2^-\}$ in fluids (Figure 9b). The composition of electrum is highly
458 sensitive to changes in the amount of Au and Ag in solutions and temperature, under
459 oxidized conditions, where Au is transported by a bisulfide complex $\{\text{Au}(\text{HS})_2^-\}$ and
460 Ag by a chloride complex $\{\text{AgCl}_2^-\}$ at Ming (Gammons and Williams-Jones, 1995). It
461 is likely that the local re-equilibrium caused by SSD in electrum, due to different

462 transport ligands and interrelated effects of physicochemical parameters of fluids (e.g.,
463 temperature and pH), resulted in opposite diffusion trends compared with electrum in
464 Au-Ag-Cu compositions in Boliden (Figure 9).

465 ***Relationship between zoning in electrum and metamorphism***

466 Post-depositional deformation and metamorphism have effects on the occurrence of
467 electrum in VMS deposits (Huston et al., 1992). In addition to coarsening the grain
468 size of electrum under metamorphic environments, the composition can also be
469 modified due to SSD reactions, particularly at higher metamorphic grade (Boyle,
470 1979; Huston et al., 1992). The SSD modification during metamorphism on electrum
471 composition has been previously reported in the Trout Lake VMS deposit (Flin Flon
472 district, Healy and Petruk, 1990). In both the Ming and Boliden deposits, silver-rich
473 electrum tends to occur along fractures in or along grain boundaries between sulfides,
474 and is intergrown with ductile-deformed sulfide minerals, in addition, shows an
475 enrichment of Hg in EPMA profiles (Figures 6 and 7). The Ag-rich electrum rim with
476 elevated Hg is considered to have formed below the peak metamorphic temperature,
477 because pervasive homogenization of Au-Ag-Hg by volume diffusion during the
478 extensive period of prograde metamorphism will erase the growth zoning in electrum
479 grains (Oberthuer and Saager, 1986). The diffusion-induced zoning with trace element
480 remobilization and incorporation at the near surface or mineral interface has been
481 documented during regional metamorphism of ore deposits (Healy and Petruk, 1990;
482 Watson, 1996; Reeder and Rakovan, 1999; Marshall et al., 2000). Thus, we consider
483 that prograde metamorphism can provide the elevated temperature and pressure to

484 form fractures that allow metamorphic fluids to dissolve the parent electrum, and to
485 mobilize trace metals (e.g., S-Fe-Cu-Zn-Pb at Ming, Se-Bi-Sb-Te-Sn-S-Zn at
486 Boliden), that are incorporated into the electrum rim by SSD reactions during the
487 retrograde metamorphic process (Figure 11).

488 **Implications**

489 This study investigated chemical zoning textures in electrum grains from the Ming
490 and Boliden VMS deposits. Electrum from the Ming deposit is zoned, with a Ag-rich
491 core that gradually shifts to a Au-rich transition zone that is in sharp contact with an
492 outer Ag-rich rim, whereas electrum from the Boliden deposit is zoned with a Au-rich
493 core with a gradational contact with a Ag-rich rim. The compositional variation and
494 textural zoning of the electrum confirm the fluid facilitated solid-state diffusion (SSD)
495 reactions within the electrum, and dissolution and reprecipitation (CDR) reactions at
496 the interface between the Au-rich zone and Ag-rich zone in electrum. Both reactions
497 can occur during the ambient greenschist to amphibolite grade metamorphism. The
498 local re-equilibrium caused by SSD, due to different transport ligands and interrelated
499 impacts of physicochemical parameters of fluids (e.g., pH and fO_2), forms different
500 compositional zoning patterns within electrum. The long-lived metamorphism event
501 probably provides the elevated temperature and fracture pathways, to allow pervasive
502 fluid infiltration to remobilize trace metals to be incorporated into electrum. This
503 study provides mineralogical evidence for different precipitation fluid conditions
504 which can result in different textural and chemical zoning patterns in electrum via
505 SSD and CDR under metamorphic conditions.

506 **Acknowledgments**

507 This study was funded by the Natural Science and Engineering Research Council of
508 Canada (NSERC), Agnico Eagle Mines Limited, Ministère de l'Énergie et des
509 Ressources Naturelles du Québec and China Scholarship Council (CSC). We thank
510 Marc Choquette (U. LAVAL) for his assistance with SEM and EPMA. Special thanks
511 to Larry Pilgrim (Rambler Metals and Mining Canada Ltd.), and Pia Fagerström (New
512 Boliden Ltd.) for providing representative gold samples for analysis. Discussion with
513 Xiaowen Huang (IGCAS) was helpful during preparation of the manuscript. We also
514 acknowledge constructive comments and suggestions from Dr. Stefanie Brueckner
515 and Dr. Brian McNulty, and editorial handling by Dr. Daniel Gregory.

516 **Figure captions**

517 **Figure 1** Simplified geological map of the Ming VMS deposit within the Pacquet
518 Complex, modified after Castonguay et al. (2009), the orebodies are projected on the
519 surface by Brueckner et al. (2016).

520 **Figure 2** Simplified geological map of the major Skellefte VMS deposit region
521 showing the location of the Boliden VMS deposit, modified after Wagner et al.
522 (2007).

523 **Figure 3** Representative ore samples from Ming (a-c) and Boliden (d-f) showing
524 mineral associations and electrum textures. (a) AnhedraI electrum occurs along the
525 boundaries of bornite and is associated with chalcocite; sample M1807. (b) AnhedraI
526 electrum intergrowths with bornite, chalcocite and cataclastic massive pyrite; sample
527 M1807. (c) Elongated electrum with light white Ag-rich rims along the boundary of
528 bornite and in contact with chalcocite; sample M1807. (d) AnhedraI electrum occurs
529 along the boundaries of arsenopyrite in quartz matrix; sample BLD210. (e) AnhedraI
530 electrum under reflected light showing a dark-yellow Au-rich core and light-yellow
531 Ag-rich rim, in contact with aurostibite; sample BLD210. (f) AnhedraI electrum
532 intergrows with recrystallized arsenopyrite and in contact with aurostibite; sample
533 BLD210. (g) Electrum intergrows with chalcopyrite and is associated with minor
534 arsenopyrite, pyrite, and trace stibnite; sample BLD-1. (h) AnhedraI electrum occurs
535 as veinlets filling in the fractures of quartz vein material with foliated pyrite; sample
536 BLD-1. (i) AnhedraI electrum intergrows with fractured pyrite and chalcopyrite;
537 sample BLD-1. Abbreviations: Apy = arsenopyrite, Aur = aurostibite, Bn = bornite,

538 Cc = chalcocite, Ccp = chalcopyrite, El = electrum, Py = pyrite.

539 **Figure 4** Backscattered electron images showing internal microstructures in zoned
540 electrum from the Ming and Boliden deposits. Electrum in (a) and (d) correspond to
541 the samples in Figures 3a and b, whereas electrum in (g) corresponds to the sample in
542 Figure 3g. (b) Example of the incongruent layers and porous texture at the interface
543 between the Au-rich transition and Ag-rich rim. The light grey layers are Au-rich,
544 whereas the dark grey layers are Ag-rich. The yellow arrows indicate the reaction
545 front with a sharp contact. (c) Variations in thickness of reprecipitated multiple
546 Ag-rich layers. (e) The yellow arrows indicate the gradational contact between the
547 Au-rich electrum core (light grey) and Ag-rich electrum rim (dark grey). (f) The sharp
548 and jagged contacts show the consequence of CDR reactions at the interface. (h)
549 Example of the gradational contact between a Au-rich core (light grey) and Ag-rich
550 rim (dark grey). (i) The yellow arrows show the gradational contact between the core
551 and rim.

552 **Figure 5** Backscattered electron images and chemical X-ray maps of zoned electrum
553 from the Ming and Boliden deposits. Electrum grains from the Ming deposit are
554 characterized by Au-poor core, Au-rich transition, and Ag-rich rim chemical zoning
555 textures which correspond to the BSE images. There are no significant Cu variations
556 in electrum from (d) and (h). (i) Example of electrum is characterized by a Au-rich
557 core and Au-depleted rim. There are no significant Fe variations in electrum from (l)
558 and (p). (m) The latter Ag-rich veins are filling in the tiny fractures in electrum and
559 fine-grained native gold grains occur along the boundary of electrum.

560 **Figure 6** Chemical variation profiles showing compositional measurement by EPMA
561 of zoned electrum from the Ming deposit. (a) shows the arranged profiles across the
562 zoned electrum. (b) and (c) show the Au and Ag area intensity of X-ray by EPMA
563 (counted by cps) along the measured line 1 and line 3 across the dark grey core, light
564 grey transition and dark grey rim. (d-f) show Au, Ag, Cu, S, and Hg contents by
565 EPMA point analyses across the zoned electrum.

566 **Figure 7** Chemical variation profiles showing the major element (Au and Ag) and
567 minor element (Cu, S, Hg) contents measured by EPMA on a zoned electrum from the
568 Boliden deposit. (e-f) show Au, Ag, Cu, S, and Hg contents determined by EPMA
569 point analyses along measured lines across the light grey core and dark grey rim.

570 **Figure 8** Multielement box and whisker plots for LA-ICP-MS trace element data
571 showing the compositional differences between the light grey and dark grey zones in
572 electrum. (a) The arranged analysis line transects the dark grey core to the light grey
573 zone on the zoned electrum in Figure 6a. The laser ablation spot size for electrum is
574 24 μm . (c) The arranged analysis line transects the light grey core to the dark grey rim
575 on the zoned electrum in Figure 7a. The laser ablation spot size for electrum is 10 μm .
576 (b) and (d) Box and whisker plots showing the chemical compositions of LA-ICP-MS
577 data of electrum. Boxes outline the 25th to 75th percentiles, and whiskers extend to the
578 5% to 95% values. Short lines within the box represent the median value, whereas
579 circles filled by white represent the average value. Red spots outside the whiskers
580 indicate the outliers beyond 5% to 95% of the dataset.

581 **Figure 9** Ternary plot showing Au-Ag-Cu compositional variations between the dark

582 grey and the light grey zones in compositionally zoned electrum. The compositional
583 data of electrum come from area intensity of X-ray by EPMA (counted by cps). (a)
584 Plot of Au-Ag-Cu variations in zoned electrum from the Ming deposit. The defined
585 dark, light, and rim zones correspond to the same area in Figure 6a. (b) Plot of
586 Au-Ag-Cu variations in the zoned electrum from the Boliden deposit. The defined
587 dark and light zones correspond to the same area in Figure 7a.

588 **Figure 10** Schematic diagram of fluid facilitated solid-state diffusion (SSD) and
589 coupled dissolution-precipitation (CDR) reactions resulting in compositional zoning
590 in electrum from the Ming and Boliden deposits. (a-c) Illustration of the zoned
591 electrum formation from the Ming deposit. (a) The parent Ag-rich electrum
592 precipitated with homogeneous compositional textures from reduced fluids. (b) With
593 increasing temperature and/or a_{S_2} , the Ag-rich electrum core was dissolved to form a
594 diffusive contact through a Au-rich fluid that likely leached S-Fe-Cu-Zn-Pb during
595 prograde metamorphism. (c) The Ag-rich electrum rim was reprecipitated on the
596 exterior of electrum from an Ag-Cu-rich fluid with increasing a_{Cu} and fO_2 during the
597 retrograde metamorphism. The repeated CDR may result in the epitaxial growth of
598 multiple Ag layers towards the margin of electrum. (d-f) illustrate the zoned electrum
599 formation from the Boliden deposit. (d) The parent Au-rich electrum precipitated with
600 homogeneous compositional textures from reduced fluids. (e) With increasing a_{H_2S}
601 and/or temperature, and decreasing pH, the Au-rich electrum core was dissolved to
602 form a gradational contact through fluids which likely leached Se-Bi-Sb-Te-Sn-S-Zn
603 during the prograde metamorphism. (f) The SSD of Ag results in coarsening of

604 electrum and forms a Ag-rich rim with decreasing temperature and increasing pH
605 during the retrograde metamorphism.

606 **Figure 11** Binary plot showing compositional variations between the core and rim in
607 zoned electrum from the Ming and Boliden deposits. The compositional data of
608 electrum come from the LA-ICP-MS analysis. (a) Plot of Au versus S + Fe + Cu + Zn
609 + Pb, showing the increasing contents of S-Fe-Cu-Zn-Pb during the dissolution of Ag
610 resulting in a Au-rich transition zone, in electrum from the Ming deposit. (b) Plot of
611 Au versus Se + Bi + Sb + Te + Sn + S + Zn, showing the increased contents of
612 Se-Bi-Sb-Te-Sn-S-Zn during the diffusion of Ag from Au-rich core from the Boliden
613 deposit.

614

615 **References**

- 616 Allen, R.L., Weihed, P., Svenson, S.-A. (1996) Setting of Zn-Cu-Au-Ag massive
617 sulfide deposits in the evolution and facies architecture of a 1.9 Ga marine volcanic
618 arc, Skellefte District, Sweden. *Economic Geology* 91: 1022-1053.
- 619 Årebäck, H., Barrett, T.J., Abrahamsson, S., Fagerström, P. (2005) The
620 Palaeoproterozoic Kristineberg VMS deposit, Skellefte district, northern Sweden,
621 part I: geology. *Mineralium Deposita* 40: 351-367.
- 622 Baheti, V.A., Kashyap, S., Kumar, P., Chattopadhyay, K., Paul, A. (2018) Solid-state
623 diffusion-controlled growth of the phases in the Au-Sn system. *Philosophical*
624 *Magazine* 98: 20-36.
- 625 Berglund, S., Ekström, T. (1980) Arsenopyrite and sphalerite as TP indicators in
626 sulfide ores from northern Sweden. *Mineralium Deposita* 15: 175-187.
- 627 Bergman Weihed, J., Bergstrom, U., Billstrom, K., Weihed, P. (1996) Geology,
628 tectonic setting, and origin of the Paleoproterozoic Boliden Au-Cu-As deposit,
629 Skellefte district, northern Sweden. *Economic Geology* 91: 1073-1097.
- 630 Billstrom, K., Weihed, P. (1996) Age and provenance of host rocks and ores in the
631 Paleoproterozoic Skellefte District, northern Sweden. *Economic Geology* 91:
632 1054-1072.
- 633 Borg, S., Liu, W., Pearce, M., Cleverley, J., MacRae, C. (2014) Complex mineral
634 zoning patterns caused by ultra-local equilibrium at reaction interfaces. *Geology* 42:
635 415-418.
- 636 Bowell, R. (1992) Supergene gold mineralogy at Ashanti, Ghana: implications for the
637 supergene behaviour of gold. *Mineralogical Magazine* 56: 545-560.
- 638 Boyle, R.W. (1979) The geochemistry of gold and its deposits. *Geol. Surv. Can. Bull.*
639 280.
- 640 Brueckner, S.M., Piercey, S.J., Layne, G.D., Piercey, G., Sylvester, P.J. (2015)
641 Variations of sulphur isotope signatures in sulphides from the metamorphosed
642 Ming Cu (- Au) volcanogenic massive sulphide deposit, Newfoundland
643 Appalachians, Canada. *Mineralium Deposita* 50: 619-640.

- 644 Brueckner, S.M., Piercey, S.J., Pilote, J.-L., Layne, G.D., Sylvester, P.J. (2016)
645 Mineralogy and mineral chemistry of the metamorphosed and precious
646 metal-bearing Ming deposit, Canada. *Ore Geology Reviews* 72: 914-939.
- 647 Brueckner, S.M., Piercey, S.J., Sylvester, P.J., Maloney, S., Pilgrim, L. (2014)
648 Evidence for syngenetic precious metal enrichment in an Appalachian
649 volcanogenic massive sulfide system: The 1806 zone, Ming mine, Newfoundland,
650 Canada. *Economic Geology* 109: 1611-1642.
- 651 Castonguay, S., Skulski, T., van Staal, C., Currie, M. (2009) New insights on the
652 structural geology of the Pacquet Harbour group and Point Rousse complex, Baie
653 Verte peninsula, Newfoundland. Newfoundland and Labrador Department of
654 Natural Resources, Geological Survey, Report 1: 147-158.
- 655 Czamanske, G.K., Desborough, G.A., Goff, F.E. (1973) Annealing history limits for
656 inhomogeneous, native gold grains as determined from Au-Ag diffusion rates.
657 *Economic Geology* 68: 1275-1288.
- 658 Desborough, G., Heidel, R., Raymond, W., Tripp, J. (1971) Primary distribution of
659 silver and copper in native gold from six deposits in the Western United States.
660 *Mineralium Deposita* 6: 321-334.
- 661 Dos Santos Alves, K., Sánchez, S.B., Barreiro, J.G., Palomares, R.M., Prieto, J.M.C.
662 (2020) Morphological and compositional analysis of alluvial gold: The Fresnedoso
663 gold placer (Spain). *Ore Geology Reviews*: 103489.
- 664 Dubé, B., Gosselin, P., Mercier-Langevin, P., Hannington, M., Galley, A. (2007)
665 Gold-rich volcanogenic massive sulphide deposits. Geological Association of
666 Canada, Mineral Deposits Division: 75-94.
- 667 Eda, K., Chin, K., Sotani, N., Whittingham, M.S. (2005) Hydrothermal synthesis of
668 potassium molybdenum oxide bronzes: structure-inheriting solid-state route to blue
669 bronze and dissolution/deposition route to red bronze. *Journal of Solid State*
670 *Chemistry* 178: 158-165.
- 671 Eda, K., Uno, Y., Nagai, N., Sotani, N., Chen, C., Whittingham, M.S. (2006)
672 Structure-inheriting solid-state reactions under hydrothermal conditions. *Journal of*
673 *Solid State Chemistry* 179: 1453-1458.

- 674 Gammons, C.H., Barnes, H. (1989) The solubility of Ag₂S in near-neutral aqueous
675 sulfide solutions at 25 to 300 C. *Geochimica et Cosmochimica Acta* 53: 279-290.
- 676 Gammons, C.H., Williams-Jones, A. (1995) Hydrothermal geochemistry of electrum;
677 thermodynamic constraints. *Economic Geology* 90: 420-432.
- 678 Gibert, F., Pascal, M.-L., Pichavant, M. (1998) Gold solubility and speciation in
679 hydrothermal solutions: Experimental study of the stability of hydrosulphide
680 complex of gold (AuHS) at 350 to 450 C and 500 bars. *Geochimica et*
681 *Cosmochimica Acta* 62: 2931-2947.
- 682 Goldsmith, J.R., Laves, F. (1954) The microcline-sanidine stability relations.
683 *Geochimica et Cosmochimica Acta* 5: 1-19.
- 684 Guisbiers, G.g., Mendoza-Cruz, R.n., Bazán-Díaz, L., Velázquez-Salazar, J.J.s.,
685 Mendoza-Perez, R., Robledo-Torres, J.A., Rodriguez-Lopez, J.-L.,
686 Montejano-Carrizales, J.M., Whetten, R.L., José-Yacamán, M. (2015) Electrum,
687 the gold–silver alloy, from the bulk scale to the nanoscale: synthesis, properties,
688 and segregation rules. *ACS nano* 10: 188-198.
- 689 Hagemann, S.G., Brown, P.E., Ridley, J., Stern, P., Fournelle, J. (1998) Ore petrology,
690 chemistry, and timing of electrum in the Archean hypozonal Transvaal lode gold
691 deposit, Western Australia. *Economic Geology* 93: 271-291.
- 692 Hannington, M., W. Bleeker, I. Kjarsgaard (1999) Sulfide mineralogy, geochemistry,
693 and ore genesis of the Kidd Creek deposit: Part II. The bornite zone. *Econ. Geol.*
694 *Mono.* 10: 225-266.
- 695 Healy, R.E., Petruk, W. (1990) Petrology of Au-Ag-Hg alloy and "invisible" gold in
696 the Trout Lake massive sulfide deposit, Flin Flon, Manitoba. *The Canadian*
697 *Mineralogist* 28: 189-206.
- 698 Hibbard, J. (1983) Geology of the Baie Verte Peninsula, Newfoundland. Mineral
699 Development Division, Department of Mines and Energy, Government
700 of Newfoundland and Labrador, 2.
- 701 Hodak, J.H., Henglein, A., Giersig, M., Hartland, G.V. (2000) Laser-induced
702 inter-diffusion in AuAg core– shell nanoparticles. *The Journal of Physical*
703 *Chemistry B* 104: 11708-11718.

- 704 Hough, R., Butt, C., Reddy, S., Verrall, M. (2007) Gold nuggets: Supergene or
705 hypogene? Australian Journal of Earth Sciences 54: 959-964.
- 706 Huang, X., Beaudoin, G. (2019) Textures and Chemical Compositions of Magnetite
707 from Iron Oxide Copper-Gold (IOCG) and Kiruna-Type Iron Oxide-Apatite (IOA)
708 Deposits and Their Implications for Ore Genesis and Magnetite Classification
709 Schemes. Economic Geology 114: 953-979.
- 710 Huston, D.L., Bottrill, R.S., Creelman, R.A., Zaw, K., Ramsden, T.R., Rand, S.W.,
711 Gemmell, J.B., Jablonski, W., Sie, S., Large, R.R. (1992) Geologic and
712 geochemical controls on the mineralogy and grain size of gold-bearing phases,
713 eastern Australian volcanic-hosted massive sulfide deposits. Economic Geology 87:
714 542-563.
- 715 Konrad-Schmolke, M., Halama, R., Wirth, R., Thomen, A., Klitscher, N., Morales, L.,
716 Schreiber, A., Wilke, F.D.H. (2018) Mineral dissolution and reprecipitation
717 mediated by an amorphous phase. Nature Communications 9: 1637.
- 718 Koski, R. (2010) Supergene ore and gangue characteristics in volcanogenic massive
719 sulfide occurrence model. US Geological Survey Scientific Investigation Report.
- 720 Larocque, A.C., Hodgson, C.J., Cabri, L.J., Jackman, J.A. (1995) Ion-microprobe
721 analysis of pyrite, chalcopyrite and pyrrhotite from the Moberly VMS deposit in
722 northwestern Quebec; evidence for metamorphic remobilization of gold. The
723 Canadian Mineralogist 33: 373-388.
- 724 Li, K., Pring, A., Etschmann, B., Xia, F., Brugger, J. (2019a) Coupling between
725 mineral replacement reactions and co-precipitation of trace elements: an example
726 from the giant Olympic Dam deposit. Ore Geology Reviews: 103267.
- 727 Li, W., Cook, N.J., Ciobanu, C.L., Xie, G., Wade, B.P., Gilbert, S.E. (2019b) Trace
728 element distributions in (Cu)-Pb-Sb sulfosalts from the Gutaishan Au-Sb deposit,
729 South China: Implications for formation of high fineness native gold. American
730 Mineralogist: Journal of Earth and Planetary Materials 104: 425-437.
- 731 Liu, J., Zhai, D., Dai, H., de Fourestier, J., Yu, C., Gu, X., Wang, Y., Yu, H., Wang, J.,
732 Liu, Z. (2017) Nanoscale Characterization of Au₂Te Grains From the Sandaowanzi
733 Gold Deposit, Northeast China. The Canadian Mineralogist 55: 181-194.

- 734 Lockington, J.A., Cook, N.J., Ciobanu, C.L. (2014) Trace and minor elements in
735 sphalerite from metamorphosed sulphide deposits. *Mineralogy and Petrology* 108:
736 873-890.
- 737 Longerich, H. (1996) Laser ablation inductively coupled plasma mass spectrometric
738 transient signal data acquisition and analyte concentration calculation. *J. Anal. At.*
739 *Spectrom.* 9: 899-904.
- 740 Lu, J., Wang, R., Hu, H., Gao, J. (2000) A new mechanism of formation of the
741 silver-rim structure on primary gold grains. *Chinese Journal of Geochemistry* 19:
742 134.
- 743 Mann, A. (1984) Mobility of gold and silver in lateritic weathering profiles; some
744 observations from Western Australia. *Economic Geology* 79: 38-49.
- 745 Marquis, P., Brown, A., Hubert, C., Rigg, D. (1990) Progressive alteration associated
746 with auriferous massive sulfide bodies at the Dumagami mine, Abitibi greenstone
747 belt, Quebec. *Economic Geology* 85: 746-764.
- 748 Marshall, B., Vokes, F., Larocque, A. (2000) Regional metamorphic remobilization:
749 upgrading and formation of ore deposits. *Reviews in Economic Geology* 11: 19-38.
- 750 Melchiorre, E., Orwin, P., Reith, F., Rea, M., Yahn, J., Allison, R. (2018) Biological
751 and geochemical development of placer gold deposits at Rich Hill, Arizona, USA.
752 *Minerals* 8: 56.
- 753 Mercier-Langevin, P., Hannington, M.D., Dubé, B., Bécu, V. (2011) The gold content
754 of volcanogenic massive sulfide deposits. *Mineralium Deposita* 46: 509-539.
- 755 Mercier-Langevin, P., McNicoll, V., Allen, R.L., Blight, J.H., Dubé, B. (2013) The
756 Boliden gold-rich volcanogenic massive sulfide deposit, Skellefte district, Sweden:
757 new U–Pb age constraints and implications at deposit and district scale.
758 *Mineralium Deposita* 48: 485-504.
- 759 Migdisov, A.A., Williams-Jones, A., Suleimenov, O. (1999) Solubility of chlorargyrite
760 (AgCl) in water vapor at elevated temperatures and pressures. *Geochimica et*
761 *Cosmochimica Acta* 63: 3817-3827.
- 762 Milidragovic, D., Beaudoin, G., Jackson, S. (2016) In-situ trace element
763 characterization of three gold reference materials using EPMA and LA-ICP-MS.

- 764 Geological Survey of Canada. Open File 8096, 1.zip file, doi, 10.4095/299097.
- 765 Oberthuer, T., Saager, R. (1986) Silver and mercury in gold particles from the
766 Proterozoic Witwatersrand placer deposits of South Africa; metallogenic and
767 geochemical implications. *Economic Geology* 81: 20-31.
- 768 Pal'yanova, G., Kolonin, G. (2007) Geochemical mobility of Au and Ag during
769 hydrothermal transfer and precipitation: Thermodynamic simulation. *Geochemistry*
770 *International* 45: 744-757.
- 771 Paton, C., Hellstrom, J., Paul, B., Woodhead, J., Hergt, J. (2011) Iolite: Freeware for
772 the visualisation and processing of mass spectrometric data. *Journal of Analytical*
773 *Atomic Spectrometry* 26: 2508-2518.
- 774 Pilote, J.-L., Piercey, S.J. (2013) Volcanostratigraphy of the 1807 zone of the Ming
775 Cu-Au volcanogenic massive-sulphide deposit, Baie Verte peninsula, northern
776 Newfoundland. *Current Research* 2013-20, 13 p.
- 777 Pilote, J.-L., Piercey, S.J., Brueckner, S.M., Grant, D. (2016) Resolving the Relative
778 Timing of Au Enrichment in Volcanogenic Massive Sulfide Deposits Using
779 Scanning Electron Microscopy-Mineral Liberation Analyzer: Empirical Evidence
780 from the Ming Deposit, Newfoundland, Canada. *Economic Geology* 111:
781 1495-1508.
- 782 Pilote, J.-L., Piercey, S.J., Mercier-Langevin, P. (2020) Evolution of the seafloor
783 hydrothermal system associated with the Ming VMS deposit, Newfoundland
784 Appalachians, and its controls on base and precious metal distribution. *Mineralium*
785 *Deposita* 55: 913-936.
- 786 Putnis, A. (2002) Mineral replacement reactions: from macroscopic observations to
787 microscopic mechanisms. *Mineralogical Magazine* 66: 689-708.
- 788 Putnis, A. (2009) Mineral replacement reactions. *Reviews in Mineralogy and*
789 *Geochemistry* 70: 87-124.
- 790 Putnis, A. (2014) Why mineral interfaces matter. *Science* 343: 1441-1442.
- 791 Putnis, A., Putnis, C.V. (2007) The mechanism of reequilibration of solids in the
792 presence of a fluid phase. *Journal of Solid State Chemistry* 180: 1783-1786.
- 793 Rea, M.A.D., Wulser, P.-A., Brugger, J., Etschmann, B., Bissett, A., Shuster, J., Reith,

- 794 F. (2019) Effect of physical and biogeochemical factors on placer gold
795 transformation in mountainous landscapes of Switzerland. *Gondwana Research* 66:
796 77-92.
- 797 Reeder, R.J., Rakovan, J. (1999) Surface structural controls on trace element
798 incorporation during crystal growth, Growth, dissolution and pattern formation in
799 geosystems. Springer, pp. 143-162.
- 800 Reith, F., Stewart, L., Wakelin, S.A. (2012) Supergene gold transformation:
801 Secondary and nano-particulate gold from southern New Zealand. *Chemical*
802 *Geology* 320: 32-45.
- 803 Robert, J.C. (2014) Mineral Dissolution and Precipitation Kinetics:: Macroscopic,
804 Microscopic and Nanoscopic Techniques. *Macla: revista de la Sociedad Española*
805 *de Mineralogía*: 20-28.
- 806 Rocholl, A.B., Simon, K., Jochum, K.P., Bruhn, F., Gehann, R., Kramar, U., Luecke,
807 W., Molzahn, M., Pernicka, E., Seufert, M. (1997) Chemical Characterisation of
808 NIST Silicate Glass Certified Reference Material SRM 610 by ICP-MS, TIMS,
809 LIMS, SSMS, INAA, AAS and PIXE. *Geostandards Newsletter* 21: 101-114.
- 810 Rosell, J.R., Serra, J.P., Aiglsperger, T., Plana-Ruiz, S., Trifonov, T., Proenza, J.A.
811 (2018) Au crystal growth on natural occurring Au—Ag aggregate elucidated by
812 means of precession electron diffraction (PED). *Journal of Crystal Growth* 483:
813 228-235.
- 814 Rosúa, F.J.C., Ruano, S.M., Hach-Alí, P.F. (2002) The three generations of gold in the
815 Palai–Islica epithermal deposit, southeastern Spain. *The Canadian Mineralogist* 40:
816 1465-1481.
- 817 Ruiz-Agudo, E., Putnis, C., Putnis, A. (2014) Coupled dissolution and precipitation at
818 mineral–fluid interfaces. *Chemical Geology* 383: 132-146.
- 819 Seward, T.M. (1973) Thio complexes of gold and the transport of gold in
820 hydrothermal ore solutions. *Geochimica et Cosmochimica Acta* 37: 379-399.
- 821 Shikazono, N., Shimizu, M. (1987) The Ag/Au ratio of native gold and electrum and
822 the geochemical environment of gold vein deposits in Japan. *Mineralium Deposita*
823 22: 309-314.

- 824 Shuster, J., Reith, F., Cornelis, G., Parsons, J.E., Parsons, J.M., Southam, G. (2017)
825 Secondary gold structures: Relics of past biogeochemical transformations and
826 implications for colloidal gold dispersion in subtropical environments. *Chemical*
827 *Geology* 450: 154-164.
- 828 Sinclair, B., Berry, R., Gemmell, J. (2000) Mineralogy and textures of the Battle Zone
829 massive sulfide lenses, Myra Falls district, British Columbia, Canada, *Volcanic*
830 *Environments and Massive Sulfide Deposits*, pp. 197-200.
- 831 Skulski, T., Castonguay, S., McNicoll, V., van Staal, C., Kidd, W., Rogers, N., Morris,
832 W., Ugalde, H., Slavinski, H., Spicer, W. (2010) Tectonostratigraphy of the Baie
833 Verte oceanic tract and its ophiolite cover sequence on the Baie Verte Peninsula.
834 Newfoundland and Labrador Department of Natural Resources, Geological Survey,
835 Report 1: 315-337.
- 836 Spear, F.S., Selverstone, J. (1983) Quantitative PT paths from zoned minerals: theory
837 and tectonic applications. *Contributions to Mineralogy and Petrology* 83: 348-357.
- 838 Spruzeniec, L., Piaolo, S., Maynard-Casely, H.E. (2017) Deformation-resembling
839 microstructure created by fluid-mediated dissolution–precipitation reactions.
840 *Nature Communications* 8: 14032.
- 841 Stefánsson, A., Seward, T. (2004) Gold (I) complexing in aqueous sulphide solutions
842 to 500 C at 500 bar. *Geochimica et Cosmochimica Acta* 68: 4121-4143.
- 843 Tenailleau, C., Pring, A., Etschmann, B., Brugger, J., Grguric, B., Putnis, A. (2006)
844 Transformation of pentlandite to violarite under mild hydrothermal conditions.
845 *American Mineralogist* 91: 706-709.
- 846 Tourigny, G., Doucet, D., Bourget, A. (1993) Geology of the Bousquet 2 Mine; an
847 example of a deformed, gold-bearing, polymetallic sulfide deposit. *Economic*
848 *Geology* 88: 1578-1597.
- 849 Vikentev, I. (2016) Selenium, tellurium and precious metal mineralogy in Uchalinsk
850 copper-zinc-pyritic district, the Urals, *IOP Conference Series: Materials Science*
851 *and Engineering*. IOP Publishing, p. 012027.
- 852 Wagner, T., Jonsson, E. (2001) Mineralogy of sulfosalt-rich vein-type ores, Boliden
853 massive sulfide deposit, Skellefte district, northern Sweden. *The Canadian*

- 854 Mineralogist 39: 855-872.
- 855 Wagner, T., Klemd, R., Wenzel, T., Mattsson, B. (2007) Gold upgrading in
856 metamorphosed massive sulfide ore deposits: Direct evidence from laser-ablation–
857 inductively coupled plasma–mass spectrometry analysis of invisible gold. *Geology*
858 35: 775-778.
- 859 Watson, E.B. (1996) Surface enrichment and trace-element uptake during crystal
860 growth. *Geochimica et Cosmochimica Acta* 60: 5013-5020.
- 861 Williams-Jones, A.E., Bowell, R.J., Migdisov, A.A. (2009) Gold in solution. *Elements*
862 5: 281-287.
- 863 Wilson, A.F. (1984) Origin of quartz-free gold nuggets and supergene gold found in
864 laterites and soils—a review and some new observations. *Journal of the Geological*
865 *Society of Australia* 31: 303-316.
- 866 Wilson, S., Ridley, W., Koenig, A. (2002) Development of sulfide calibration
867 standards for the laser ablation inductively-coupled plasma mass spectrometry
868 technique. *Journal of Analytical Atomic Spectrometry* 17: 406-409.
- 869 Xia, F., Brugger, J., Chen, G., Ngothai, Y., O’Neill, B., Putnis, A., Pring, A. (2009)
870 Mechanism and kinetics of pseudomorphic mineral replacement reactions: A case
871 study of the replacement of pentlandite by violarite. *Geochimica et Cosmochimica*
872 *Acta* 73: 1945-1969.
- 873 Xiong, G., Clark, J.N., Nicklin, C., Rawle, J., Robinson, I.K. (2014) Atomic diffusion
874 within individual gold nanocrystal. *Scientific reports* 4: 6765.
- 875 Yokoyama, K., Takeuchi, S., Nakai, I., Tsutsumi, Y., Sano, T., Shigeoka, M.,
876 Miyawaki, M., Matsubara, M. (2011) Chemical Compositions of Electrum Grains
877 in Ore and Placer Deposits in the Japanese Islands. National Museum of Nature
878 and Science.
- 879 Zachariáš, J., Němec, M., O’Driscoll, B. (2017) Gold to aurostibite transformation and
880 formation of Au-Ag-Sb phases: the Krásná Hora deposit, Czech Republic.
881 *Mineralogical Magazine* 81: 987-999.
- 882 Zhao, J., Brugger, J., Grundler, P.V., Xia, F., Chen, G., Pring, A. (2009) Mechanism
883 and kinetics of a mineral transformation under hydrothermal conditions: Calaverite

884 to metallic gold. American Mineralogist 94: 1541-1555.
885 Zhao, J., Brugger, J., Xia, F., Ngothai, Y., Chen, G., Pring, A. (2013)
886 Dissolution-reprecipitation vs. solid-state diffusion: Mechanism of mineral
887 transformations in sylvanite, (AuAg)₂Te₄, under hydrothermal conditions.
888 American Mineralogist 98: 19-32.
889

Table 1 EPMA results of electrum grains from the Ming and Boliden deposits

		Internal texture	Number of analyses	Chemical composition (wt%)					Mineral association
				Au	Ag	Cu	Hg	S	
Ming	Electrum with zoning	Silver rich rim	3	b.d.l-0.99	84.70-99.29	0.17-2.11	0.01-6.24	0.05-0.13	Ccp, Bn, Cc, Py
		Rim	4	62.13-69.01	33.06-39.85	0.21-1.43	0.07-0.22	0.02-0.04	
		Transition	26	71.62-78.76	20.74-30.09	0.03-0.45	b.d.l.-0.16	0.01-0.36	
		Core	13	65.35-77.42	21.71-35.00	0.03-1.59	b.d.l.-6.77	0.02-0.13	
	Electrum without zoning		8	69.15-90.56	10.54-30.73	0.25-2.85	b.d.l.-0.18	0.04-0.26	
Boliden	Electrum with zoning	Rim	17	47.89-69.43	24.54-46.08	b.d.l.-5.07	b.d.l.-2.77	0.02-4.46	Apy, Ccp, Py, Aur, (Cu)-Pb-Sb sulfosalts
		Transition	5	54.90-65.37	32.17-40.43	0.06-0.30	1.39-2.08	0.06-0.07	
		Core	21	62.01-89.97	6.04-34.67	b.d.l.-0.21	b.d.l.-1.68	0.01-0.10	
	Electrum without zoning		25	45.74-92.23	6.37-50.79	b.d.l.-0.05	b.d.l.-3.03	0.02-0.15	

*Note: dataset is from Supplementary data 2. B.d.l. indicates values below the detection limits. Apy: arsenopyrite, Aur: aurostibite, Bn: bornite, Cc: chalcocite, Ccp: chalcopyrite, Py: pyrite

Figure 1

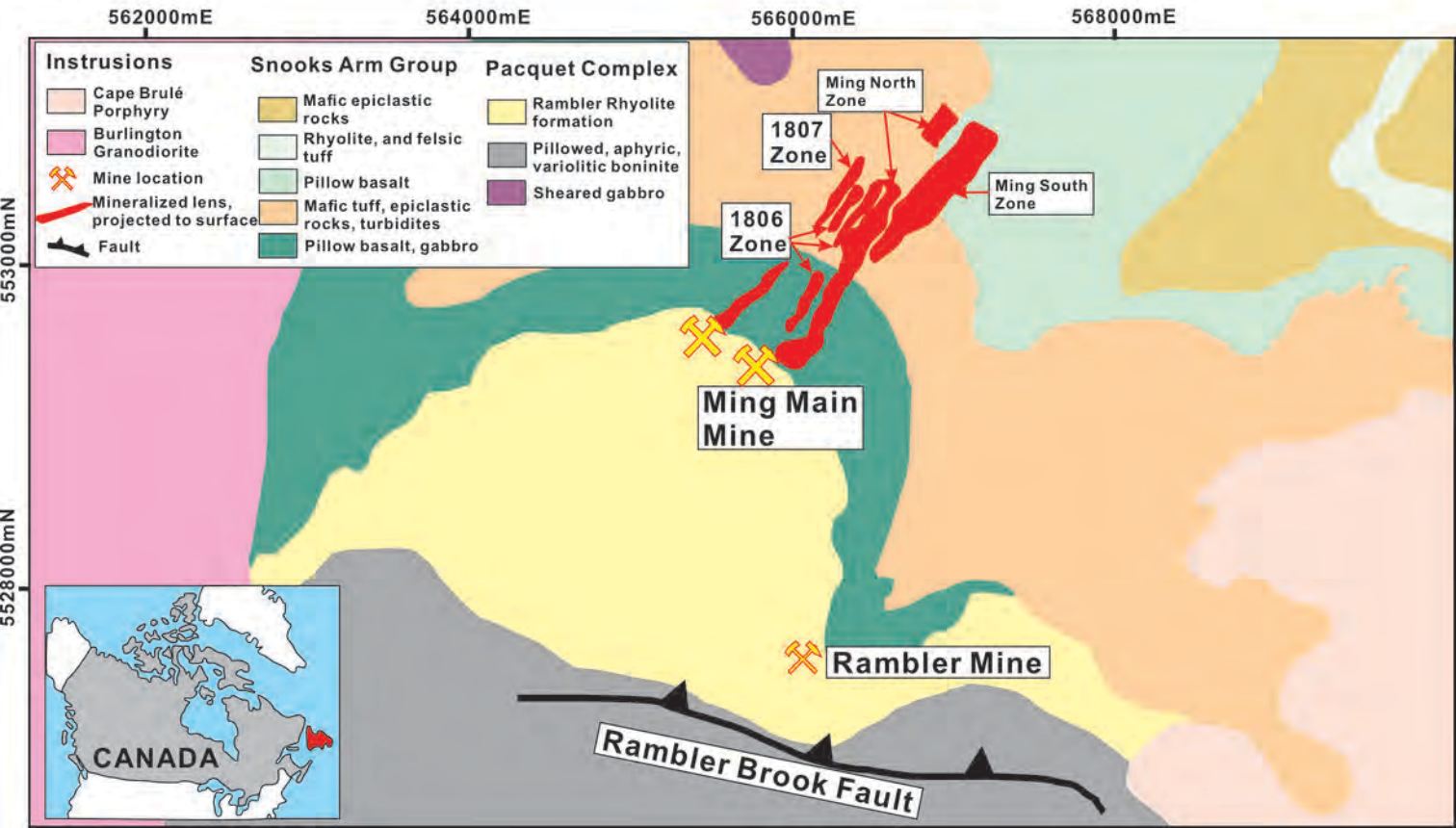


Figure 2

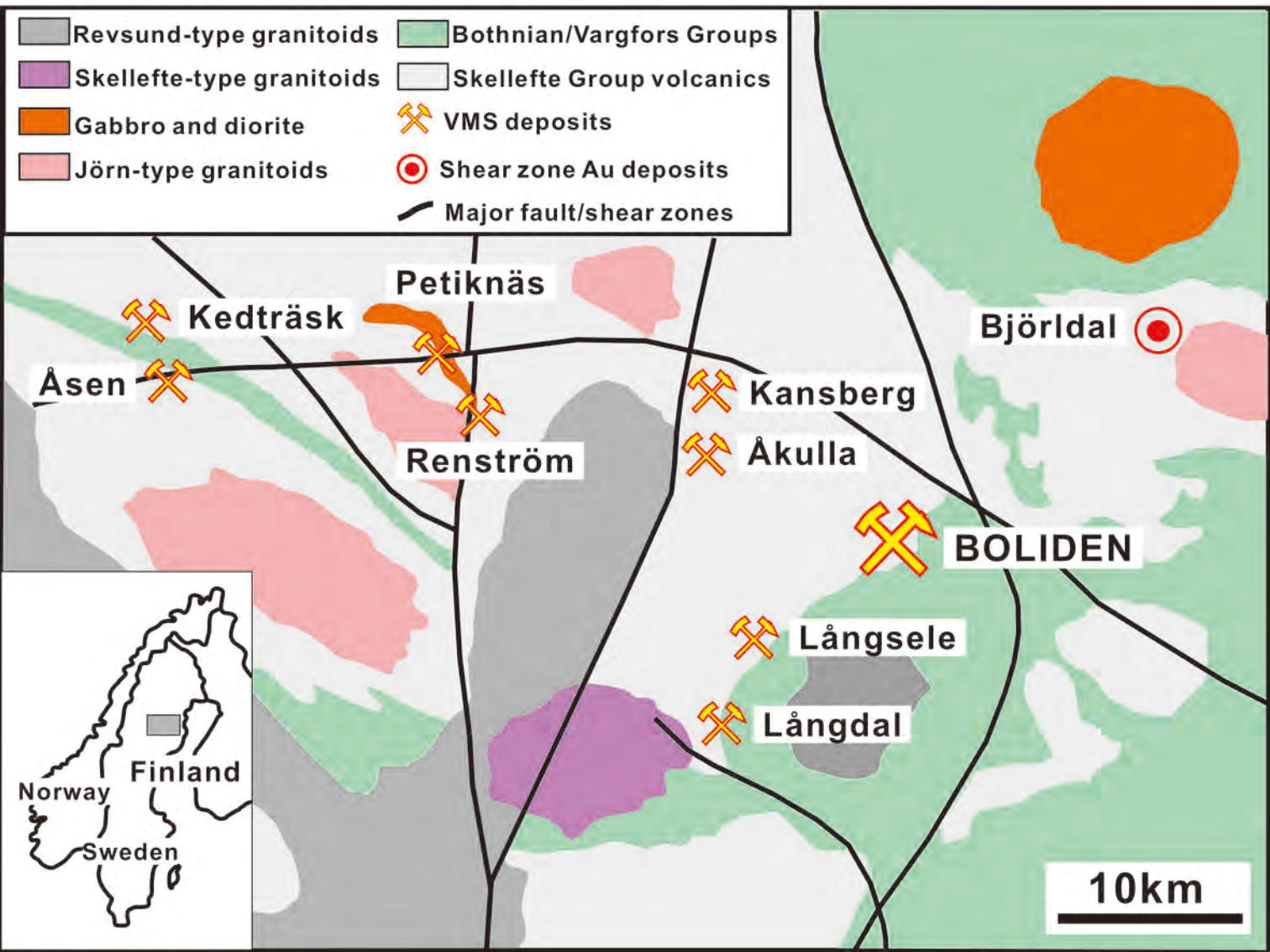


Figure 3

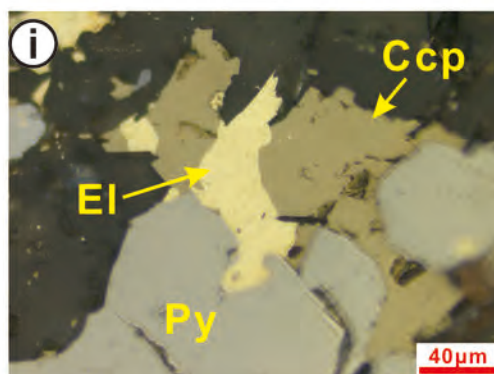
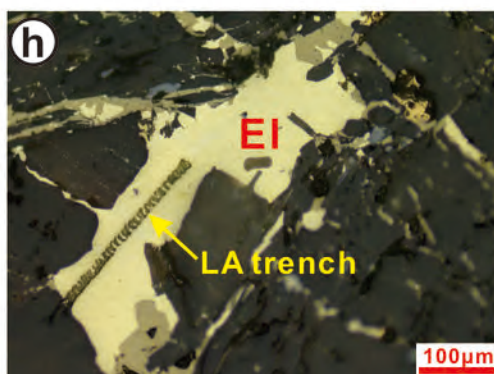
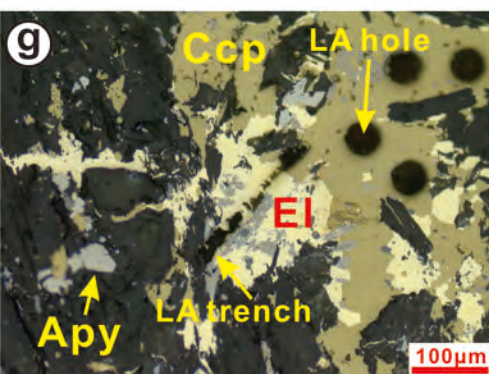
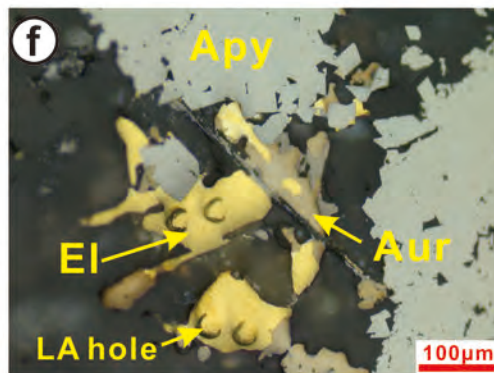
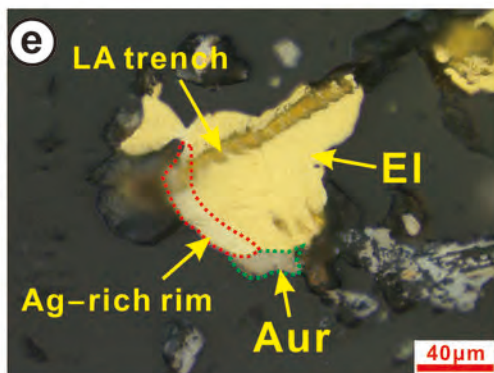
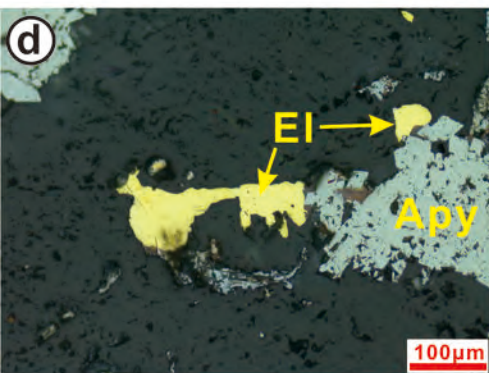
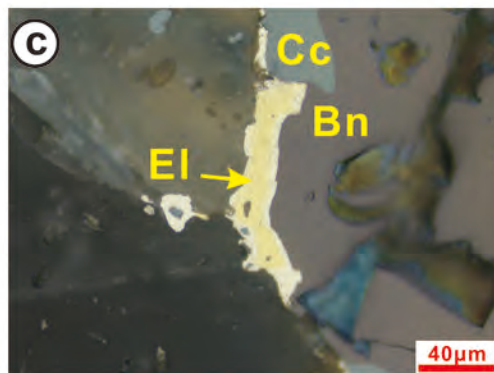
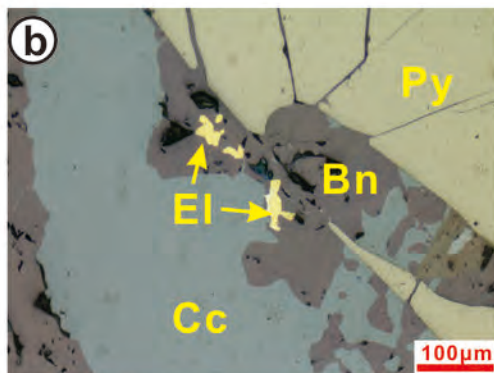
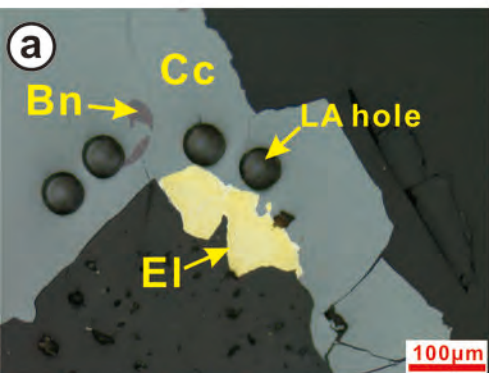


Figure 4

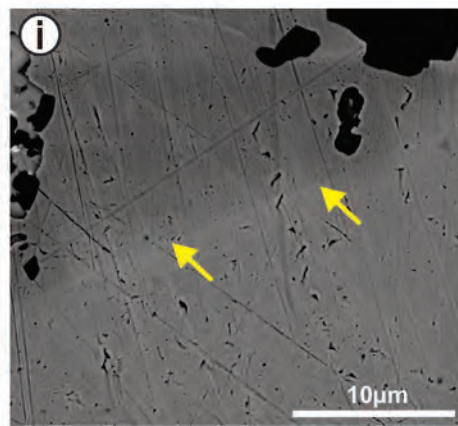
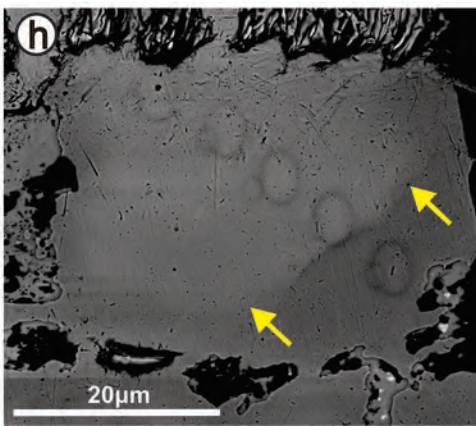
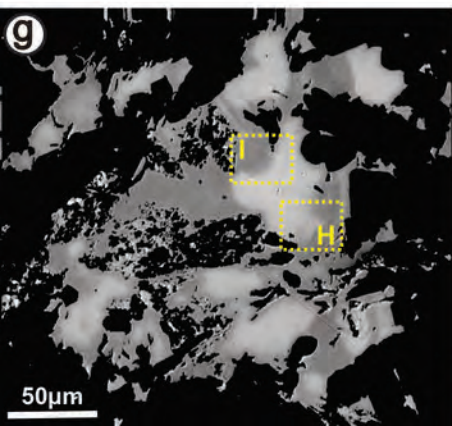
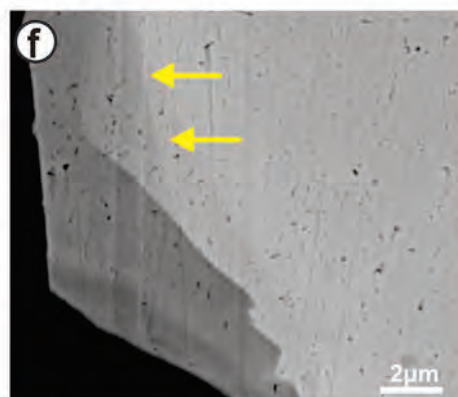
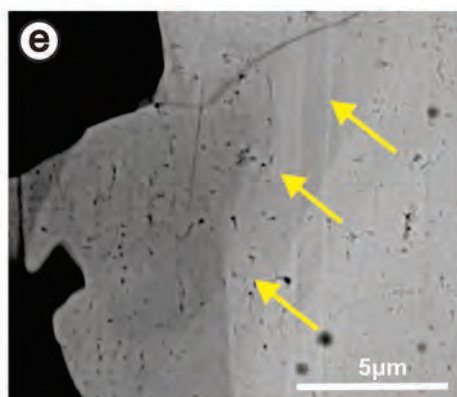
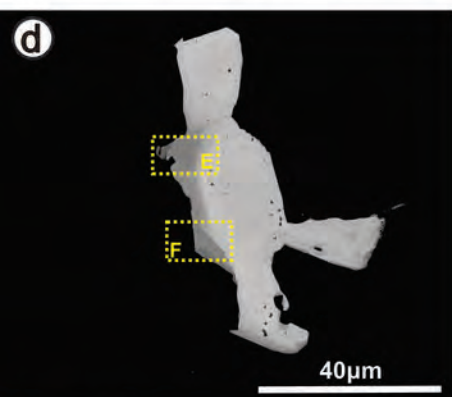
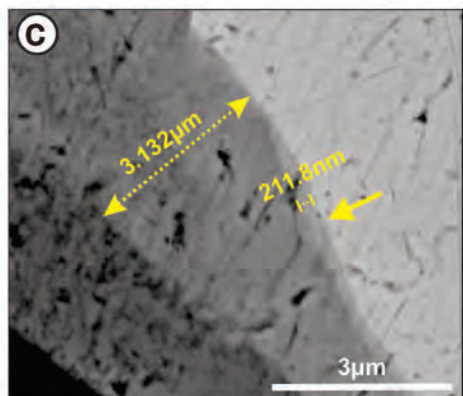
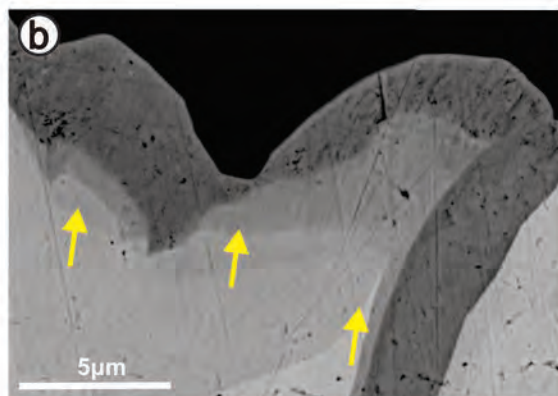
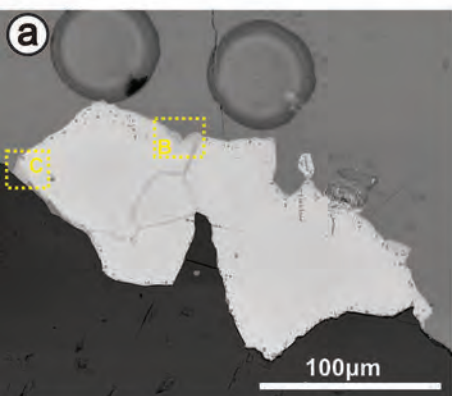


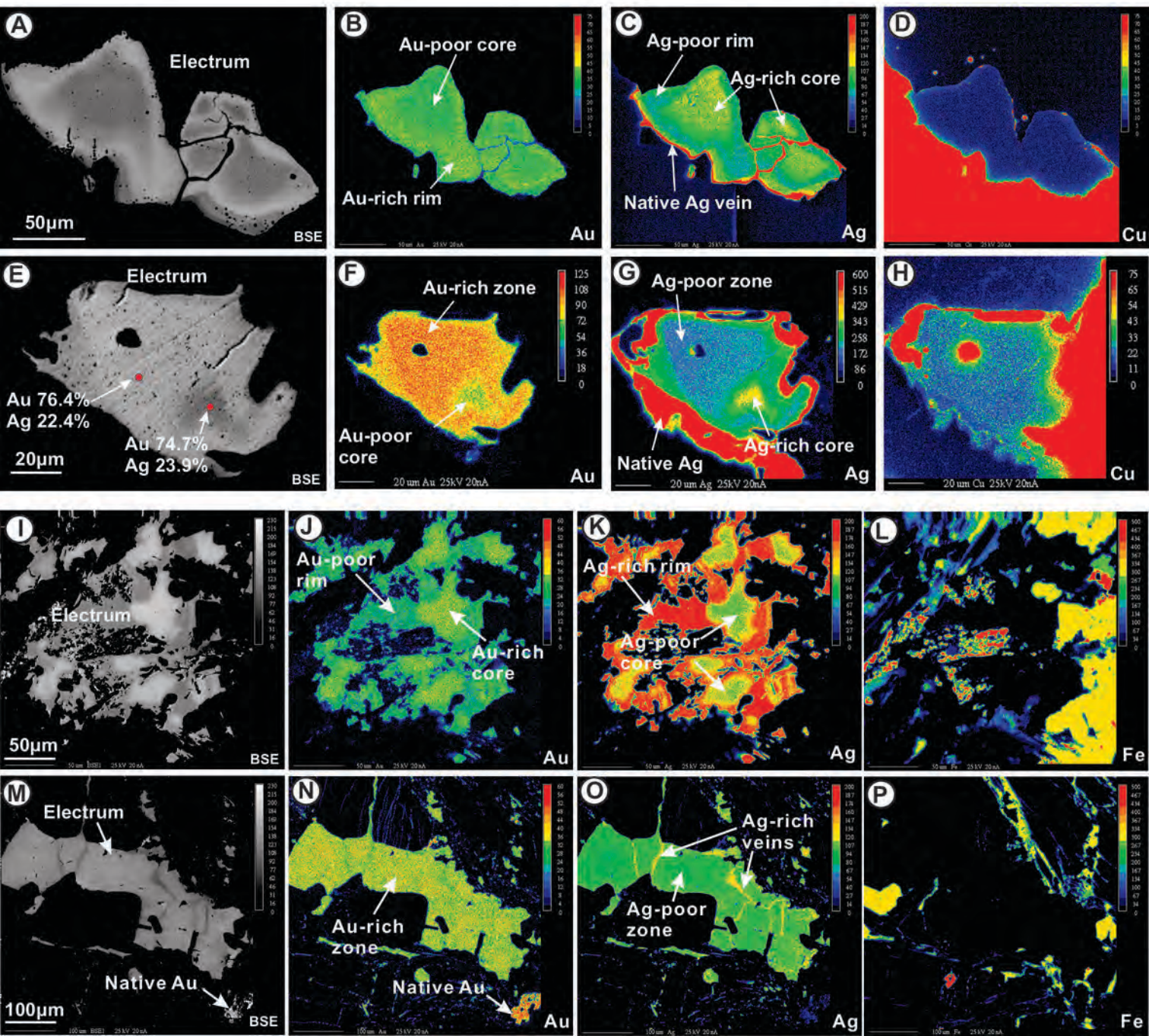
Figure 5

Figure 6

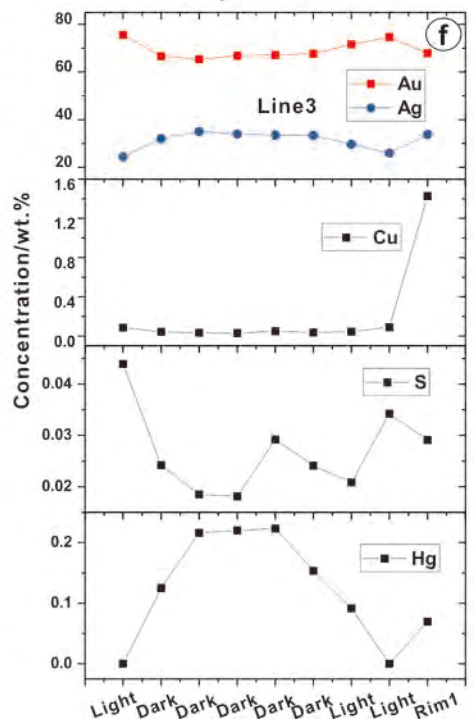
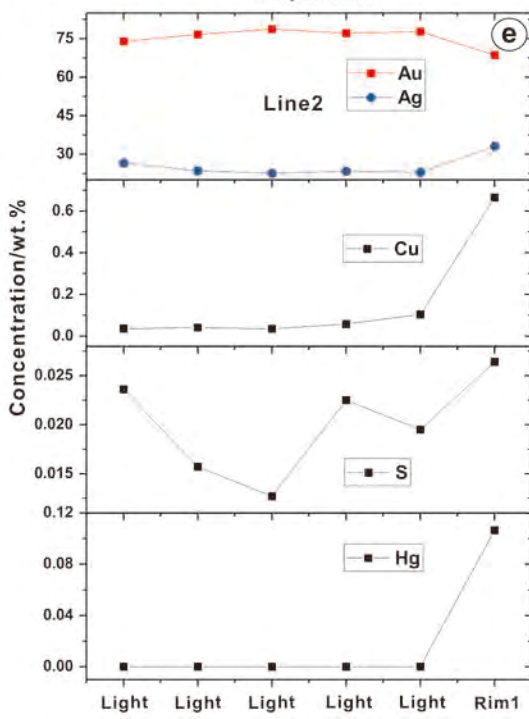
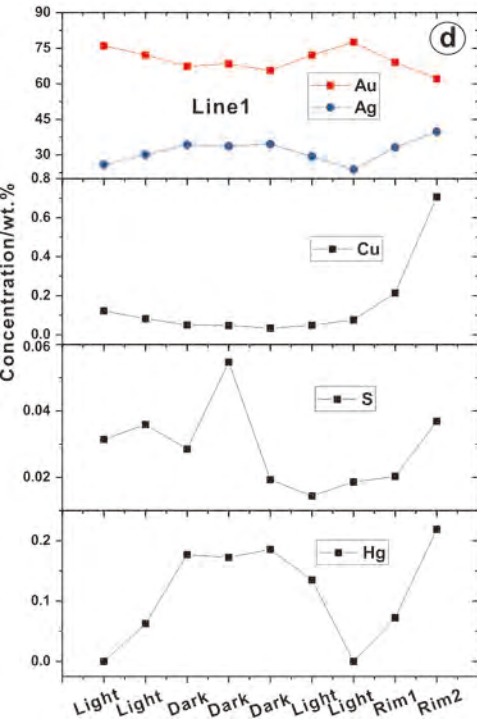
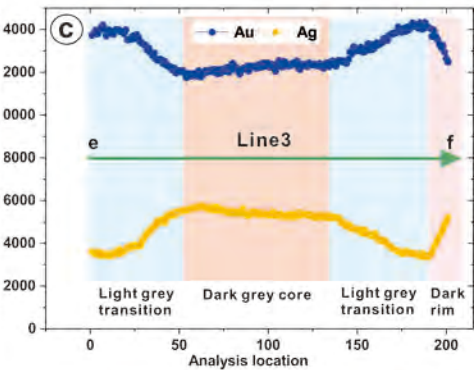
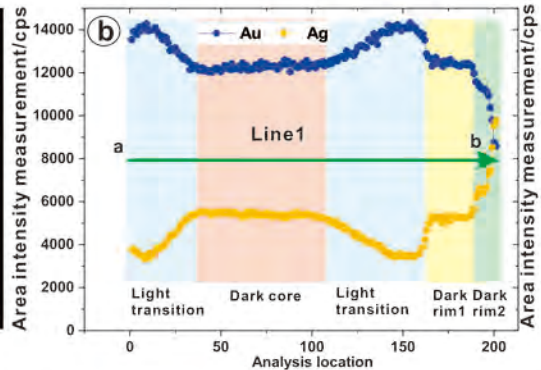
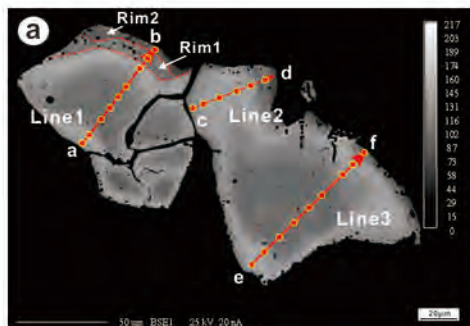


Figure 7

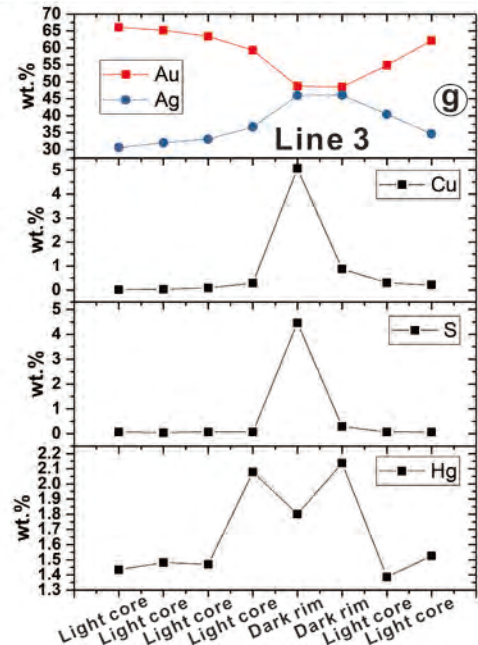
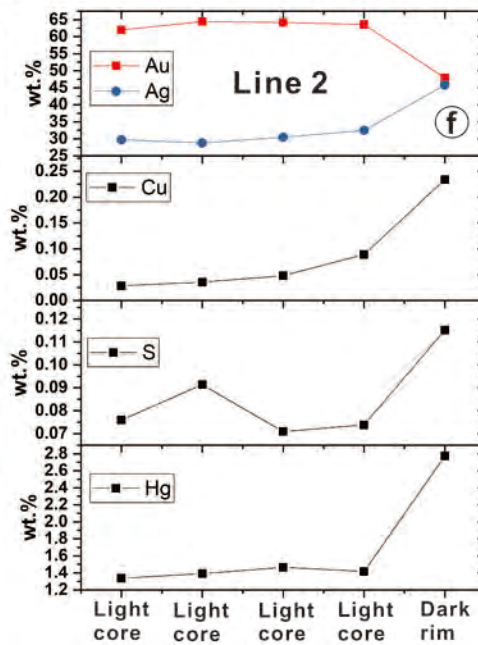
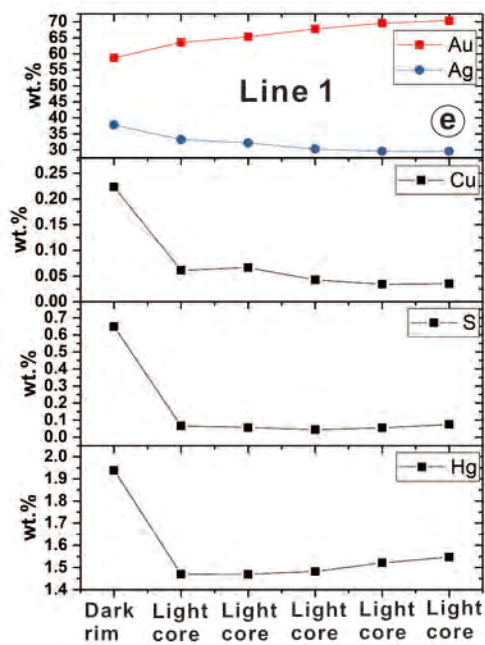
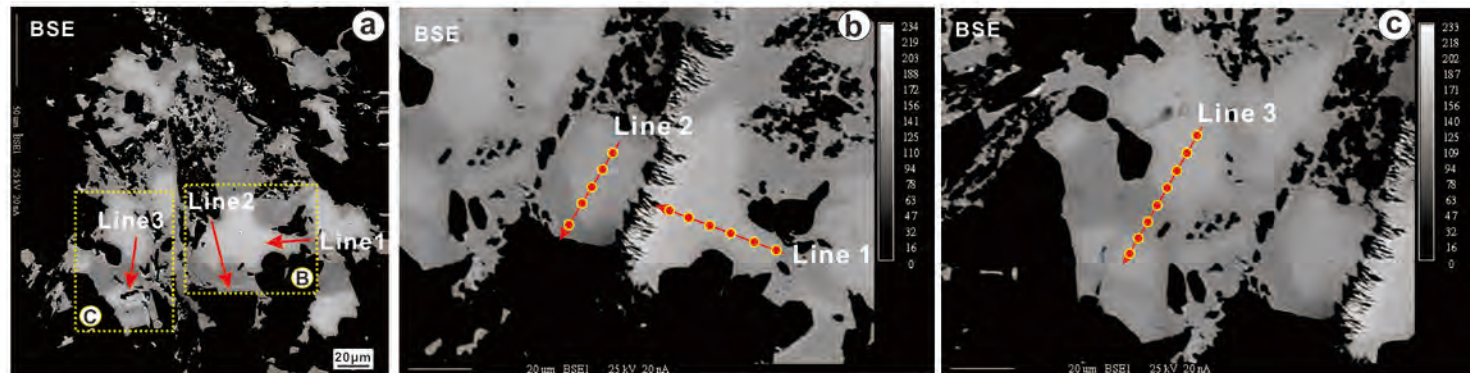


Figure 8

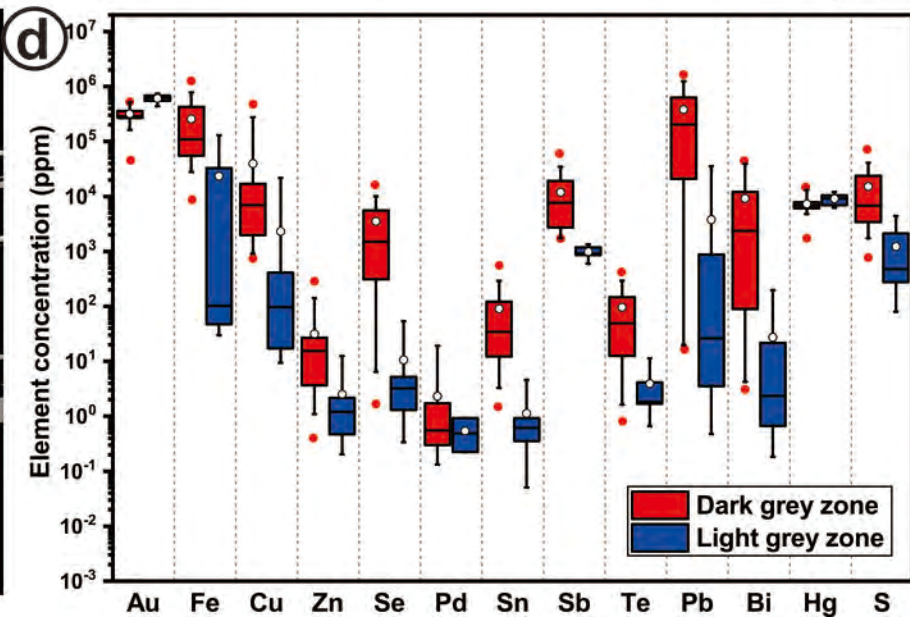
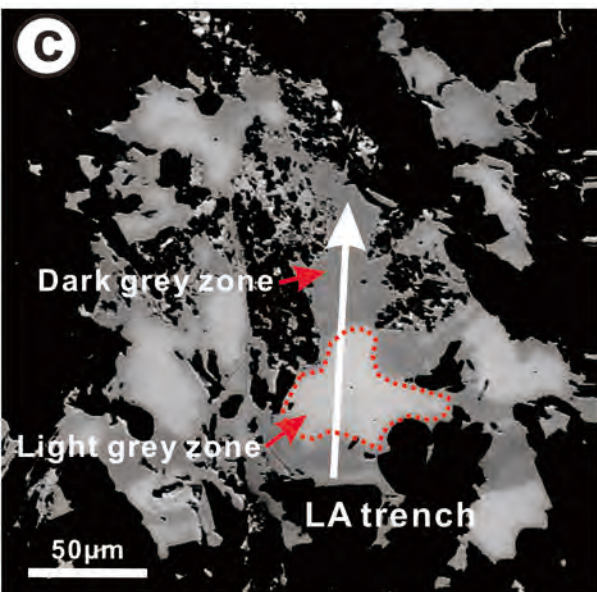
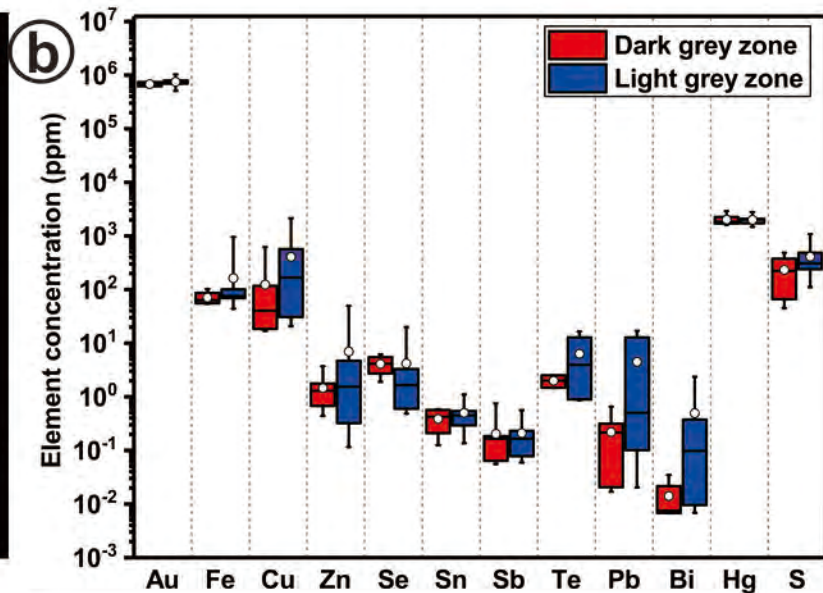
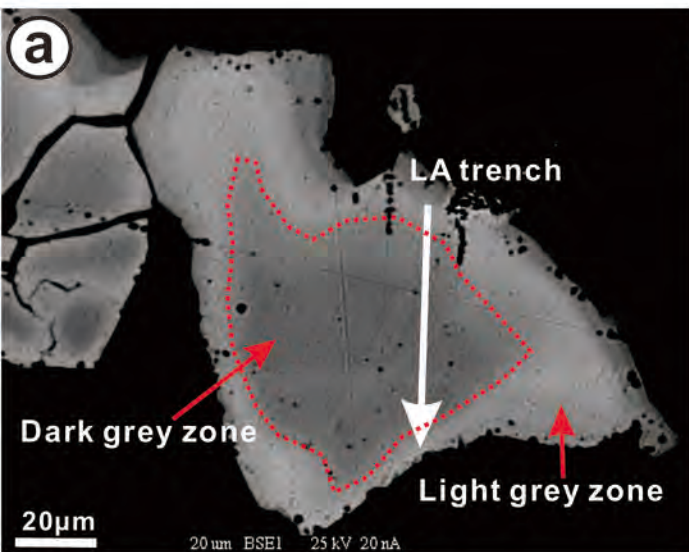


Figure 9

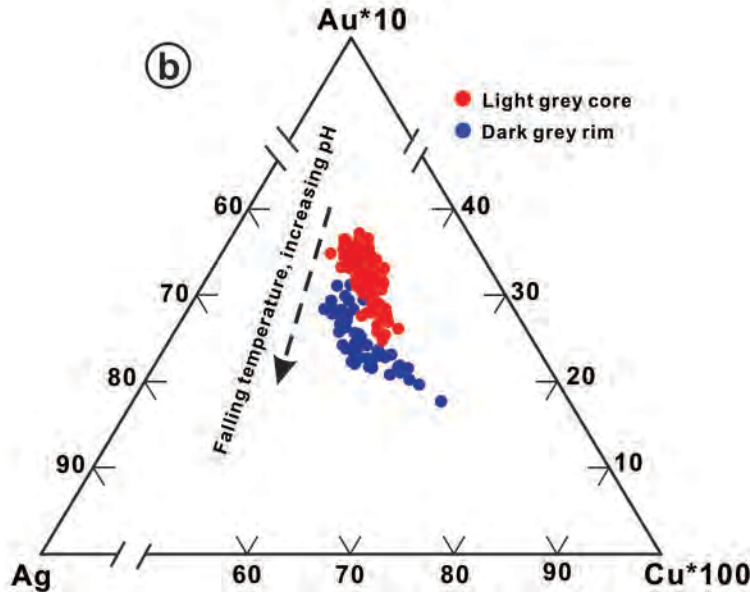
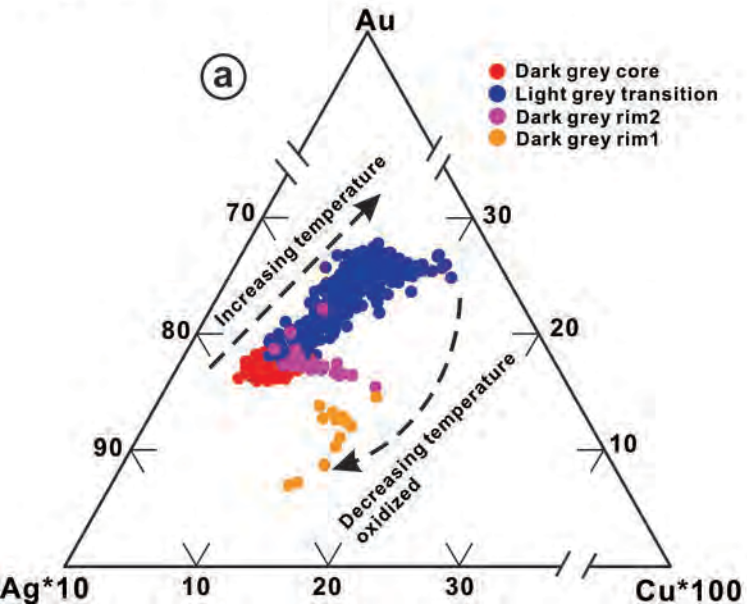


Figure 10

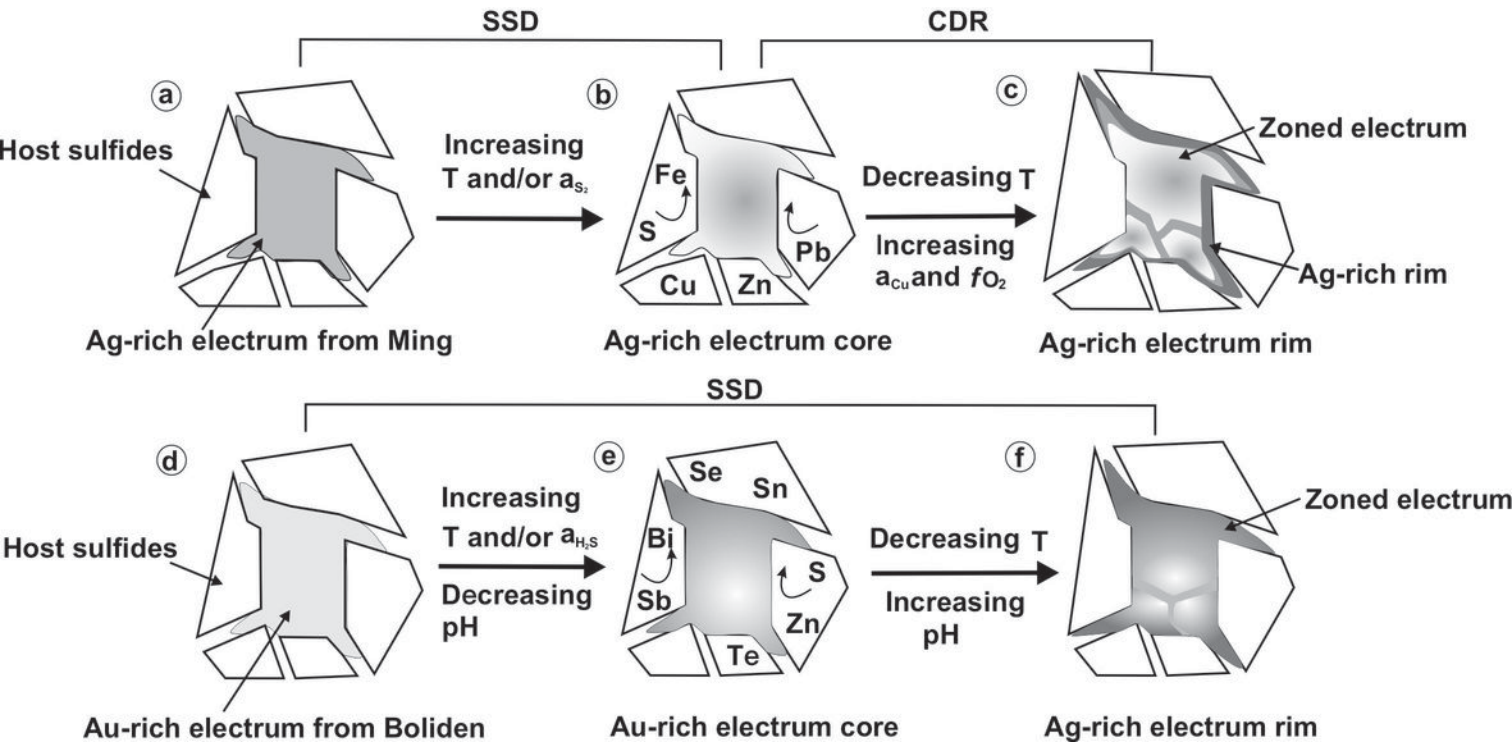


Figure 11

